Earth's Future

RESEARCH ARTICLE
10.1029/2025EF006094

Impacts of Idealized Land Use and Land Management Changes on Weather Extremes in West Africa

Souleymane Sy[1], Joel Arnault[1,2], Jan Bliefernicht[1], Benjamin Quesada[3], Gregory Duveiller[4], Abdel Nassirou Yahaya Seydou[5], Francis E. Oussou[6], Benjamin Fersch[2], Patrick Laux[2], Verena Huber-García[7], Andreas Hirner[7], and Harald Kunstmann[1,2,8]

[1]University of Augsburg, Institute of Geography, Chair for Regional Climate and Hydrology, Augsburg, Germany, [2]Institute of Meteorology and Climate Research IMK-IFU Karlsruhe Institute of Technology, Garmisch-Partenkirchen, Germany, [3]Universidad del Rosario, School of Sciences and Engineering, "Interactions Climate-Environment (ICE)" Research Group, Earth System Sciences Program, Bogotá, Colombia, [4]Max Planck Institute for Biogeochemistry, Jena, Germany, [5]Kwame Nkrumah University of Science and Technology, Kumasi, Ghana, [6]Federal University of Technology, Akure (FUTA), Akure, Nigeria, [7]Deutsches Zentrum für Luft- und Raumfahrt (DLR), German Aerospace Center, Munich, Germany, [8]University of Augsburg, Center for Climate Resilience Augsburg, Augsburg, Germany

Key Points:

- Deforestation of the West African savanna region significantly intensifies temperature extremes (up to 0.45 ± 0.04°C) and increases drought lengths
- Afforestation with mixed or evergreen forests mitigates extreme heat, while woody savanna or savanna may worsen it due to albedo induced warming effects
- Afforestation leads to increased mean and extreme precipitation, more frequent wet days, and shorter drought durations

Supporting Information:

Supporting Information may be found in the online version of this article.

Correspondence to:

S. Sy and H. Kunstmann,
souleymane.sy@uni-a.de;
harald.kunstmann@kit.edu

Citation:

Sy, S., Arnault, J., Bliefernicht, J., Quesada, B., Duveiller, G., Seydou, A. N. Y., et al. (2025). Impacts of idealized land use and land management changes on weather extremes in West Africa. *Earth's Future*, *13*, e2025EF006094. https://doi.org/10.1029/2025EF006094

Received 15 FEB 2025
Accepted 3 OCT 2025

Author Contributions:

Conceptualization: Souleymane Sy
Data curation: Souleymane Sy, Verena Huber-García, Andreas Hirner
Formal analysis: Souleymane Sy, Joel Arnault
Funding acquisition: Harald Kunstmann
Investigation: Souleymane Sy
Methodology: Souleymane Sy, Benjamin Fersch
Project administration: Harald Kunstmann
Resources: Souleymane Sy
Software: Souleymane Sy

Abstract Land-based mitigation strategies, such as afforestation and avoided deforestation, are critical to achieving the Paris Agreement's goal of limiting global warming to 1.5°C or 2°C. However, the biophysical impacts of anthropogenic land use and land cover change (LULCC), particularly deforestation and afforestation, on extreme weather events in West Africa remain poorly understood at the regional scale. In this study, we present the first high-resolution LULCC experiments (at 3 km resolution, covering 2012–2022) using the advanced fully coupled atmosphere-hydrology WRF-Hydro model system to assess the potential impacts of idealized land use and land management scenarios on extreme events in the West African savannah region. By analyzing 18 extreme weather indices, we show that deforestation significantly affects temperature extremes (up to 0.45 ± 0.04°C), with effects on regional rainfall extremes being approximately twice as pronounced as those on mean rainfall conditions, along with a significant increase in the number of dry days. Conversely, afforestation generally leads to increases in both mean and extreme precipitation, along with fewer dry days and shorter drought durations. Notably, afforestation produces contrasting responses in temperature extremes depending on vegetation type: converting grassland to mixed or evergreen forest reduces extreme heat via increased transpiration, while conversion to savanna or woody savanna may intensify heat extremes due to albedo-induced warming effects.

Plain Language Summary West Africa is currently experiencing extensive agricultural intensification associated with rapid population growth. Those anthropogenic land use and land-cover changes (LULCC) can have significant impacts on regional climate but also on extreme weather events, posing high vulnerability to human, natural, and economic systems. However, the effects of LULCC (including deforestation and afforestation) on extreme events in West Africa remain largely unexplored at the regional scale, lacking consensus. This study employs high-resolution LULCC simulations (3 km resolution, 2012–2022) using an advanced coupled atmosphere-hydrology model to evaluate the impacts of land cover transition scenarios on extreme events in the West African Savanna. The results indicate that deforestation significantly influences temperature extremes, while it consistently affects regional rainfall extremes—about twice as much as mean rainfall changes—and substantially increases the number of dry days. Conversely, afforestation scenarios generally lead to increases in both mean and extreme precipitation, fewer dry days, and shorter drought durations. Notably, afforestation with mixed or evergreen forests mitigates extreme heat through enhanced plant transpiration. However, certain forest types, such as woody savanna or savanna, can exacerbate heat extremes due to albedo-induced warming effects.

1. Introduction

Anthropogenic land use and land cover change (LULCC) can have a significant impact on regional climate, as well as extreme weather events affecting health, energy, agriculture, and other socio-economic sectors (IPCC-SRCCL, 2019; IPCC-SREX, 2012; Sillmann et al., 2013; Sy & Quesada, 2020). LULCC influences the climate system through both biophysical and biogeochemical pathways. Biophysical effects involve changes to surface properties such as albedo, evapotranspiration, and roughness (Mahmood et al., 2014; Perugini et al., 2017;

Supervision: Jan Bliefernicht, Patrick Laux, Harald Kunstmann
Validation: Souleymane Sy
Visualization: Souleymane Sy
Writing – original draft: Souleymane Sy
Writing – review & editing: Souleymane Sy, Joel Arnault, Jan Bliefernicht, Benjamin Quesada, Gregory Duveiller, Abdel Nassirou Yahaya Seydou, Francis E. Oussou, Benjamin Fersch, Patrick Laux, Verena Huber-García, Andreas Hirner, Harald Kunstmann

Yahaya Seydou et al., 2025), whereas biogeochemical effects result from alterations to atmospheric concentrations of greenhouse gases (e.g., CO_2, CH_4 and N_2O), which are primarily driven by land use and management practices (Bonan, 2008; Guug et al., 2025).

Afforestation has been proposed as a land-based solution to mitigate global warming (Cook-Patton et al., 2020; Doelman et al., 2020; Duveiller et al., 2020; Palmer, 2021). Large-scale afforestation projects like the Great Green Wall Initiative have been proposed and initiated to mitigate climate change impacts in West Africa (Ingrosso & Pausata, 2024; Smiatek & Kunstmann, 2023). This initiative seeks to restore nearly 100 million hectares of forest by 2030 (UNCCD, 2024). However, climate mitigation strategies, such as Reducing Emissions from Deforestation and Forest Degradation (REDD+), primarily emphasize some biogeochemical mechanisms but often overlook their biophysical effects. While biogeochemical effects are evaluated globally and form the basis of agreements like the Paris Climate Agreement, biophysical effects are usually neglected despite their significant regional impacts (Duveiller et al., 2020; Mahmood et al., 2014; Perugini et al., 2017; Spracklen et al., 2018; Sy et al., 2017; Sy & Quesada, 2020). These biophysical effects are particularly relevant for local climate mitigation, as they can be immediately felt by people living nearby, up to 50 km from the forests (Cohn et al., 2019).

Beyond its ability to reduce atmospheric greenhouse gases (Cook-Patton et al., 2020; Palmer, 2021), afforestation can moderate temperature extremes, reduce drought lengths (Abiodun et al., 2013; Cao et al., 2023; Ingrosso & Pausata, 2024; Schwaab et al., 2020), and enhance extreme precipitation (Camara et al., 2022; Diba et al., 2018; Ingrosso & Pausata, 2024; Saley et al., 2019; Smiatek & Kunstmann, 2023). Although climate models provide a better understanding of the consequences of afforestation (Bonan, 2008; Perugini et al., 2017), the debates related to the net effects of afforestation on local/regional climate have been ongoing for several years (Arnault et al., 2023; Breil et al., 2021; Duveiller et al., 2018a; Ingrosso & Pausata, 2024; Perugini et al., 2017). For example, the biophysical effects of afforestation can have the potential to either counteract or enhance the cooling impact associated with its carbon sequestration (Arora & Montenegro, 2011; Bala et al., 2007; Pongratz et al., 2010; Windisch et al., 2021). In other words, afforestation may also induce surface warming due to its lower albedo, while cooling effects can also be observed through increased heat dissipation and enhanced evapotranspiration efficiency (Bonan, 2008; Duveiller et al., 2018b). These effects also depend on various factors, including (a) the background climate conditions resulting in contrast temperature responses across different latitudes (Duveiller et al., 2018b; Perugini et al., 2017); (b) altitudes and/or local orography characteristics (Abera et al., 2024; Zeng et al., 2021); and (c) seasons (Ingrosso & Pausata, 2024). This climate dependence is evident not only in the immediate effects but also in the evolving responses of afforestation over time in response to greenhouse gas-induced warming. However, model responses show large disagreement (Abiodun et al., 2013; Camara et al., 2022; Ingrosso & Pausata, 2024; Odoulami et al., 2019; Schwaab et al., 2020; Smiatek & Kunstmann, 2023), and the full benefits and potential tradeoffs of afforestation, particularly its biophysical impacts on climate extremes, remain largely unexplored. This is especially true in West Africa, where studies are often based on coarse-resolution simulations (e.g., Smiatek & Kunstmann, 2023) and/or limited to a few extreme indices (e.g., Camara et al., 2022; Diba et al., 2018; Ingrosso & Pausata, 2024; Odoulami et al., 2019). While climate models can elucidate the effects of afforestation, the model-based results are still subject to uncertainties in representing local biophysical processes (Ge et al., 2021; Sy et al., 2017; Sy & Quesada, 2020). One challenge is that land-atmosphere interactions in climate models are typically simplified, especially at the river basin scale (Arnault et al., 2021, 2023; Ndiaye et al., 2024). Studies using coupled atmospheric-hydrological models, such as the WRF-Hydro model, have shown that incorporating surface and subsurface lateral water flow enhances runoff simulation and modifies the atmospheric water cycle, generally leading to increased evapotranspiration and precipitation (e.g., Arnault et al., 2021, 2023; Fersch et al., 2020; Furnari et al., 2022; Rummler et al., 2019). However, this local positive feedback is often neglected in deforestation and afforestation-based modeling studies (Abiodun et al., 2013; Achugbu et al., 2023; Camara et al., 2022; Diba et al., 2018; Ingrosso & Pausata, 2024; Smiatek & Kunstmann, 2023; Sy et al., 2017; Sy & Quesada, 2020).

Here, for the first time, high-resolution idealized LULCC (deforestation and afforestation) simulations at 3 km, covering the period from 2011 to 2022, were conducted using the fully coupled WRF-Hydro model system (Arnault et al., 2023; Mortey et al., 2024; Ndiaye et al., 2024). This system incorporates surface and subsurface lateral water flow while dynamically describing vegetation (Arnault et al., 2016, 2023; Gochis et al., 2020). Notably, the high-resolution experiments under different idealized LULCC scenarios with WRF-Hydro enable the capture of fine-scale biophysical effects of LULCC on weather extremes, accounting for surface terrestrial hydrological processes (Mortey et al., 2024; Ndiaye et al., 2024). This study addresses three main scientific

10.1029/2025EF006094

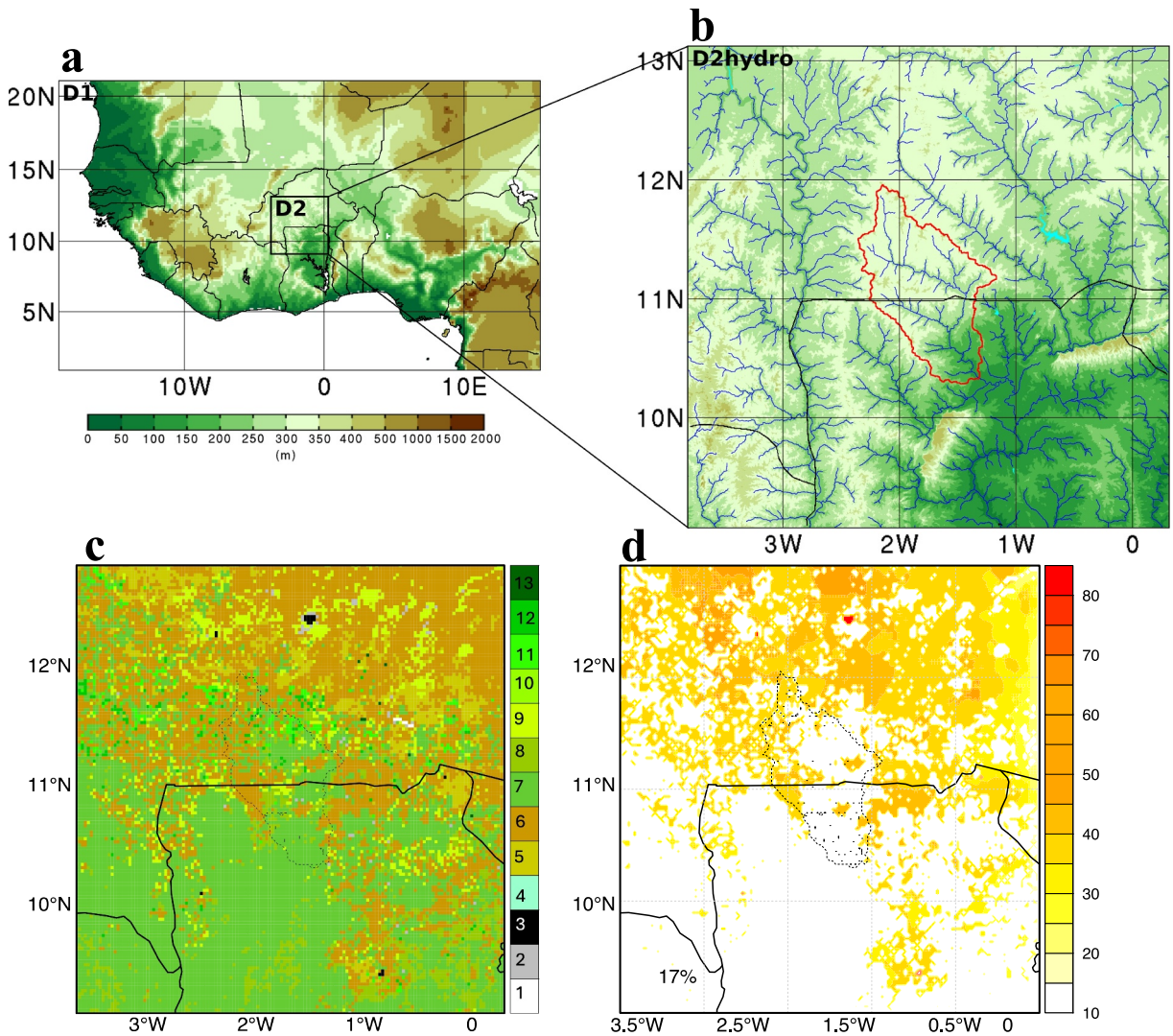

Figure 1. (a) Topography height (in meters above sea level) is depicted for the outer and inner domains, D1 and D2, respectively, at resolutions of 15 and 3 km. (b) Sub-domain (D2hydro) at a resolution of 300 m is coupled with D2 for water routing computations (Arnault et al., 2023; Mortey et al., 2024; Ndiaye et al., 2024). The black rectangle indicates the location of D2, while the red and blue contour lines represent the Sissili River basin location and main rivers, respectively. The topography color scale provided by the color bar on the bottom side is consistent for both panels. (c) Dominant land cover categories as used in the WRF-Hydro system, based on MODIS-IGBP 21 category classification for our study area. The land cover categories are represented as follows: 1. Water, 2. Barren or sparsely vegetated, 3. Urban and built-up, 4. Cropland/natural vegetation mosaic, 5. Cropland, 6. Grassland, 7. Savannas, 8. Woody savannas, 9. Open shrublands, 10. Closed shrublands, 11. Mixed Forests, 12. Deciduous Needle/Broadleaf forests, 13. Evergreen Needle/Broadleaf Forests. (d) The simulated regional distribution of the land use change fraction (%) between the CTL and NoLCC experiments. The regionally averaged land use change fraction between CTL and NoLCC is shown in the lower-left corner of the panel.

questions: (a) What are the potential benefits and tradeoffs of afforestation on climate extremes in West Africa? (b) What are the underlying biophysical mechanisms behind the LULCC-induced responses? (c) To what extent does the WRF-Hydro system enable the derivation of improved extreme climate characteristics?

2. Materials and Methods

2.1. Study Area

The study area is situated in the West African savanna region, as depicted in Figures 1a and 1b. It spans Southwest Burkina Faso and Northern Ghana, located between 9° and 13°N and 3.5° and 0.5°W. The local climate is influenced by the West African Monsoon (WAM). It is characterized by distinct periods: a dry phase in winter (December-January-February), a rainy phase in summer (July-August-September), and two transitional periods.

The annual precipitation ranges from 900 to 1,200 mm (Nicholson, 2013), primarily from mesoscale convective systems, leading to highly variable spatiotemporal rainfall patterns, causing significant challenges for rainfed agricultural activities (Waongo et al., 2024). The region also experiences significant multidecadal precipitation variability, leading to frequent large-scale droughts, including the severe Sahel droughts of the 1970s and 1980s (Masih et al., 2014; Nicholson, 2013). Temperatures generally range from 22°C to 34°C, with maximum values reaching up to 40°C during the dry season in March and April, primarily due to the influence of dry, northeasterly Harmattan winds (Nyadzi et al., 2022). Daily maximum temperatures typically occur around 15:00 UTC, while minimum temperatures are usually recorded around 06:00 UTC (Guug et al., 2025) during the cooler months of December, January, and February, when they can drop to as low as 18°C. The selection of the study area is driven by several key factors: (a) its location within a tropical West African savanna region; (b) the ongoing agricultural intensification (Bliefernicht et al., 2018; Potapov et al., 2022), which underscores the potential advantages of afforestation policies in the context of climate-smart agriculture (Rosenstock et al., 2016); and (c) the presence of significant watersheds (see Figure 1b), particularly the Sissili River Basin (12,800 km^2), which serves as a focal research site for the West African Science Service Centre on Climate Change and Adapted Land Use (WASCAL) (Arnault et al., 2016; Bliefernicht et al., 2018; Hingerl et al., 2025; Mortey et al., 2024; Nadolski et al., 2024).

2.2. Coupled WRF-Hydro Model Setup

To simulate the response of climate extremes to LULCC, we used the advanced WRF-Hydro model system (Arnault et al., 2023; Gochis et al., 2020; Mortey et al., 2024). This system integrates the Weather Research and Forecasting model (WRF; version 4.4; Skamarock et al., 2019) with the WRF-Hydro hydrological module (version 5.2; Gochis et al., 2020). The coupled system solves atmospheric motion equations on a three-dimensional grid and provides parameterization options for subgrid-scale processes, including radiation, turbulence, cumulus convection, cloud microphysics, and terrestrial hydrology (e.g., Arnault et al., 2021, 2023; Fersch et al., 2020; Rummler et al., 2019). Our WRF-Hydro setup (see Table S1 in Supporting Information S1) is similar to (Mortey et al., 2024) and has been further optimized based on previous studies in West Africa and neighboring regions (e.g., Arnault et al., 2023; Ndiaye et al., 2024). These studies evaluated different microphysical, cumulus, longwave radiation, and planetary boundary layer (PBL) schemes (Arnault et al., 2023; Mortey et al., 2024; Ndiaye et al., 2024), which allows us to select some adequate scheme configurations for this region. However, exploring the sensitivity of our analysis to an exhaustive range of WRF-Hydro model system schemes falls outside the scope of this study.

In this paper, the simulations are conducted on two regional domains (Figure 1). The outer domain (D01) covers significant portions of West Africa at a resolution of 15 km with 50 vertical levels up to 10 hPa (Figure 1a). Initial conditions and lateral boundaries are constrained by ERA5 reanalysis data provided by ECMWF (Hersbach et al., 2020). The inner domain, driven by the outer domain through one-way nesting, covers an area of 450 km × 450 km at a resolution of 3 km, utilizing a scale-aware convective parameterization scheme, Grell & Freitas, 2014), significantly improving the representation of heavy rainfall events (Park et al., 2022, 2024). Both domains use 60-s timesteps for numerical stability. The inner domain incorporates lateral terrestrial flow using the WRF-Hydro hydrological module (Gochis et al., 2020) and the community Noah land surface model with Multi-Parameterization (Noah-MP), which includes a dynamic vegetation component. This configuration enables the simulation of vegetation carbon assimilation and soil carbon decomposition processes by activating the dynamic vegetation options. Soil moisture dynamics are represented within a 2-m soil column, divided into four layers (Niu et al., 2011). This module is crucial for updating upward energy and water vapor fluxes at the lower boundary of the simulated atmosphere (Gochis et al., 2020). The WRF-Hydro routing modules are activated within the inner domain through a coupling mechanism between the 3-km grid and a 300 m subgrid (Figure 1b), created using the WRF-Hydro Pre-processing Tool and digital elevation data from the HydroSHEDS database (Lehner et al., 2008). Each timestep, surface water, and soil moisture variables from Noah-MP are disaggregated on the subgrid, routed, and then aggregated back to the Noah-MP grid (Gochis et al., 2020). The disaggregation factor is updated at the end of each timestep, ensuring the inner domain reflects the averaged impact of terrestrial water transport resolved on the fine subgrid (Arnault et al., 2023).

2.3. Validation Data

The model performance was evaluated using observational and reanalysis data sets for precipitation, temperature, and leaf area index (LAI). This evaluation ensures the suitability of the model for LULCC experiments

Table 1
Description of the Land Cover Categories and Idealized Afforestation Experiments, Labeled as $AFF_{X/Y}$, Representing Specific Vegetation Cover Transition Scenarios, Where X and Y Denote the Baseline and Target Forest Types, Respectively, as Classified Under the MODIS International Geosphere-Biosphere Programme (IGBP) Scheme

Land-use category	Considered forest types and descriptions	Land cover transition scenarios	Idealized experiments
Grassland (GRA) Lands with herbaceous types of cover. Tree and shrub cover is less than 10%. Permanent wetlands lands with a permanent mixture of water and herbaceous or woody vegetation	Woody Savannah (WOS): Lands with herbaceous and other understory systems, and with forest canopy cover between 30% and 60%. The forest cover height exceeds 2 m	GRA → WOS	$AFF_{GRA/WOS}$
Grassland (GRA) Lands with herbaceous types of cover. Tree and shrub cover is less than 10%. Permanent wetlands lands with a permanent mixture of water and herbaceous or woody vegetation	Savannah (SAV): Lands with herbaceous and other understory systems, with forest and canopy cover between 10% and 30%. The forest height cover exceeds 2 m	GRA → SAV	$AFF_{GRA/SAV}$
Grassland (GRA) Lands with herbaceous types of cover. Tree and shrub cover is less than 10%. Permanent wetlands lands with a permanent mixture of water and herbaceous or woody vegetation	Mixed Forests (MXF): Lands dominated by trees with a percent cover >60% and height exceeding 2 m. Consists of tree communities with interspersed mixtures or mosaics of evergreen and deciduous forests. None of the forest types exceeds 60% of landscape	GRA → MXF	$AFF_{GRA/MXF}$
Grassland (GRA) Lands with herbaceous types of cover. Tree and shrub cover is less than 10%. Permanent wetlands lands with a permanent mixture of water and herbaceous or woody vegetation	Evergreen Broadleaf Forests (EBF): Lands dominated by broad leaf woody vegetation with a percentage cover >60% and height exceeding 2m. Almost all trees and shrubs remain green year-round. Canopy is never without foliage	GRA → EBF	$AFF_{GRA/EBF}$

Note. The target forest types include woody savanna (WOS), savanna (SAV), mixed forest (MXF), and evergreen forest (EBF).

(Noblet-Ducoudré et al., 2012; Sy et al., 2017). Precipitation data from CHIRPS-V2 (Funk et al., 2015) combine satellite infrared and in situ station data, providing daily quasi-global estimates on a 0.05° grid since 1981. Temperature data were obtained from the ERA5-Land reanalysis (Muñoz-Sabater et al., 2021), which provides ∼9 km resolution and hourly land variables. LAI variability was assessed using the Copernicus Land Monitoring Service (CLMS) data sets, which provide 300 m global LAI data every 10 days since 2014 (Fuster et al., 2020). Data gaps due to cloud cover were addressed with a gap-filled LAI version smoothed with a Savitzky-Golay filter (Savitzky & Golay, 1964). All data sets were resampled to 3 km × 3 km (9 km × 9 km for temperature) resolution using bilinear interpolation for model comparison.

2.4. Experimental Setup

Simulations were conducted from 1 January 2011 to 1 January 2023, with the first year excluded for model spin-up. However, following previous studies in West Africa (e.g., Abiodun et al., 2008; Achugbu et al., 2022; Boone et al., 2016; Diba et al., 2018; Glotfelty et al., 2021; Saley et al., 2019; Wang et al., 2016), the length of our simulation period (11 years; 2012–2022) is assumed to be sufficient to reduce the influence of model internal variability (e.g., Lorenz et al., 2016) on the mean differences calculated between the different experiments. Overall, five idealized experiments, each representing a specific land cover transition scenario in the Sudan Savanna of Burkina Faso and Ghana (see Table 1), were performed alongside a reference simulation (CTL experiment). To ensure comparability, all simulations were conducted using the same model configuration, as detailed in Section 2.2 and Table S1 in Supporting Information S1, under present-day climate forcing conditions. In the control (CTL) experiment, the default WRF land cover map from the MODIS product MCD12Q1 (version 6.0; Sulla-Menashe et al., 2019) based on the International Geosphere-Biosphere Program (IGBP) 21-category classification (see Figure 1c) was used, representing present-day conditions with a 2015 land cover map. According to the MODIS land cover classification (Figure 1c), the dominant land cover types in the study area are savanna—particularly in northwestern Ghana—and grassland, which is mainly found in southern Burkina Faso. Together, savanna and grassland account for approximately 40% and 38% of the total grid cells, respectively, making them the most prevalent land cover categories. Woody savanna, open shrubland, and cropland each

account for 6% of the total land cover pixels. Mixed Forests (MXF), consisting of tree communities with interspersed mosaics of evergreen and deciduous species, cover 1% of the area. Smaller proportions of our study area are classified as Evergreen Broadleaf Forests (EBF) (0.5%) and deciduous broadleaf forests (0.7%) (see Table 1 for the description of land cover categories).

To explore the potential regional biophysical impacts of deforestation on climate extremes - in particular, changes in land surface properties such as surface albedo and evapotranspiration efficiency - this study compares the climate of a maximally forested region (referred to as the "NoLCC" experiment) with that of a present-day simulation (referred to as control "CTL" experiment) representing a predominantly deforested landscape (see Figure 1c). The vegetation map for the idealized maximally forested scenario was developed by modifying the CTL land cover map (see Figure 1c). Grid cells with at least 80% coverage by urban, built-up, or agricultural land (cropland and grassland) were reclassified as tropical broadleaf evergreen forest, which represents the potential natural vegetation for tropical regions (Davin & Noblet-Ducoudré, 2010; Findell et al., 2017; Glotfelty et al., 2021; Odoulami et al., 2019). For areas that did not meet this criterion, the dominant forest type from the nearest neighboring grid cells was assigned. While this extreme scenario is not intended to reflect a realistic LULCC, it serves as a conceptual framework to explore the biophysical effects of deforestation caused by changes in the physical properties of the land surface (Davin et al., 2020; Davin & Noblet-Ducoudré, 2010) and their influence on climate extremes in the West African savanna region. Furthermore, this study builds on previous studies that have investigated climate model responses to deforestation (e.g., converting forest to grassland) using idealized LCC scenarios (e.g., Boysen et al., 2020; Davin et al., 2020; Davin & Noblet-Ducoudré, 2010; Findell et al., 2017; X. Luo et al., 2022; Winckler et al., 2017). Moreover, as shown in Figure 1d, the simulated spatial pattern of the extent of land use change fraction between the CTL and NoLCC experiments (averaging about 17%) is consistent with the observed expansion of agricultural land (about 19%; see Potapov et al., 2022) in the Sudan savannah belt of Burkina Faso and Ghana, despite uncertainties and limitations in identifying actual LULCC. Discrepancies in LULCC maps are often due to errors in satellite data acquisition, processing limitations, extraction methods, and unsuitable legend classes. Current satellite-derived vegetation maps struggle to represent LULCC accurately, particularly in West Africa, where agricultural areas are often misclassified (Boone et al., 2016; Rahimi et al., 2021). Distinguishing between crop and pasture fractions is challenging, especially when livestock graze on crop fields after harvest (Bliefernicht et al., 2018; Rahimi et al., 2021).

Beyond the CTL and NoLCC experiments, four idealized afforestation experiments were conducted to investigate the potential biophysical effects of afforestation scenarios, which are much less studied in the literature (Jia et al., 2019). Each experiment involves a specific vegetation transition, that is, from grassland (GRA) to a forest type as defined by the IGBP classification scheme: woody savanna (WOS), savanna (SAV), mixed forest (MXF) and evergreen broadleaf forests (EBF). In other words, in these afforestation experiments, the total grid cell previously occupied by grassland (which accounts for 38% of the total grid points; see Figure 1c) is converted to a forest type (i.e., either WOS, SAV, MXF, or EBF) (see Table 1 for more details). In the following, the four afforestation experiments are referred to as $AFF_{X/Y}$ (i.e., $AFF_{GRA/WOV}$, $AFF_{GRA/SAV}$, $AFF_{GRA/MXF}$, and $AFF_{GRAS/EBF}$), where the subscripts X/Y indicate a given vegetation cover transition scenario from grassland (X) to a forest type (Y). Consequently, the difference between $AFF_{X/Y}$ and CTL experiments (i.e., $AFF_{X/Y}$ minus CTL) reflects the pure biophysical effects of an idealized afforestation scenario. In our afforestation experiments, the percentage of grid points previously classified as water, urban, built-up, desert, barren, and cropland remained unchanged due to the challenges associated with predicting the future changes of these land cover categories. This approach has also been used to prevent vegetation expansion into areas unsuitable for tree growth.

It is worth noting that although numerous studies have demonstrated increasing annual precipitation and more frequent rainy days in West Africa over the past two decades, leading to a partial recovery in precipitation levels (Salack et al., 2018; Sanogo et al., 2015; Sylla et al., 2016) and future projections suggesting higher rainfall in the central and eastern Sahel - particularly in Burkina Faso, Ghana, and southern Niger by the late 21st century (Deme et al., 2017; Sylla et al., 2016), this study does not assess the feasibility of an afforestation experiment in this region. Challenges include local climatic conditions, such as the ability of the environment to sustain a newly "transformed" ecosystem in terms of water availability and soil fertility constraints. In addition, planting tree species in dry environments remains a challenge, even when local species, such as savanna, are used (Elagib et al., 2021). Nonetheless, the vegetation types used in our afforestation experiments are coherent with the region and consistent with those analyzed in previous studies conducted in West Africa. These include deciduous and/or EBF (e.g., Abiodun et al., 2013; Bamba et al., 2019; Glotfelty et al., 2021; Ingrosso & Pausata, 2024; Odoulami

et al., 2019), woody savannas (e.g., Smiatek & Kunstmann, 2023) and savannas (e.g., Odoulami et al., 2019; Smiatek & Kunstmann, 2023). Additionally, recent observations of increasing seasonal greenness across large areas of the Sahel (e.g., Herrmann et al., 2005; Jury, 2018) suggest significant shifts in vegetation dynamics, which may be related to the partial recovery of rainfall. While these ongoing greening trends and the associated changes in surface moisture dynamics may influence land–atmosphere interactions, investigating the causes of these changes and their wider impact on regional climate extremes is beyond the scope of this study.

To enhance the robustness of the results and address model uncertainties, two additional simulations—analogous to CTL and NoLCC experiments—were performed using only the WRF model (i.e., excluding the WRF-Hydro hydrological module) while maintaining the same physical parameterizations (see Table S1 in Supporting Information S1). The results showed similar overall patterns, although the WRF-Hydro system produced slightly more pronounced signals, particularly for specific indices (not shown). In addition, to account for inter-annual variability in the model, particularly for precipitation responses to LULCC - which are subject to greater uncertainty due to a lower signal-to-noise ratio (Laux et al., 2017; Spracklen et al., 2018) - all simulations were also run in ensemble mode. This approach involved five ensemble members (i.e., $n = 5$ realizations per experiment) with perturbed initial atmospheric boundary conditions (Laux et al., 2017), with the ensemble mean representing the model response.

2.5. Detection of Robust LULCC Signals

Area-weighted means for each temperature and precipitation index were calculated regionally to assess the contributions of LULCC scenarios to extreme weather indices. Detecting signals from small perturbations, such as the effects of LULCC, poses the challenge of distinguishing true forcing signals from noise arising from internal climate variability (Winckler et al., 2017). To address this, we adopted the methodology proposed by (Lorenz et al., 2016) to assess the statistical significance of simulated changes in climate modeling experiments. The significance of each simulated change was assessed using the Mann-Whitney-Wilcoxon (MWW) rank test (Lorenz et al., 2016; Wu et al., 2014) on two sets of 11-year simulations (2012–2022) comparing CTL with NoLCC or $AFF_{X/Y}$ experiments. Results were considered significant if the MWW test yields a p-value < 0.05 (95% confidence level). The MWW test was chosen for its robustness and suitability for non-normally distributed data, as opposed to the Student's t-test (Sy et al., 2021). Additionally, the non-parametric Kendall rank correlation test (Croux & Dehon, 2010) was applied to estimate correlations, as it is less sensitive to outliers than Pearson and Spearman tests (Diouf et al., 2022).

2.6. Weather Extremes Indices

This study specifically focuses on mean temperature and precipitation (Tmean and Pmean), along with a comprehensive set of 18 extreme temperature and precipitation indices from the total of 27 indices defined by the World Meteorological Organization Expert Team on Climate Change Detection and Indices (ETCCDI; https://www.wcrp-climate.org/etccdi). These indices were included to comprehensively represent extreme temperature and precipitation across the region. They were computed based on daily rainfall and minimum and maximum temperatures and applied to all CTL, NoLCC, and $AFF_{X/Y}$ simulations. The selection of these 18 extreme weather indices (see Table S2 in Supporting Information S1) was based on their significance in social decision-making processes.

2.7. Surface Energy Balance Decomposition

To explore the mechanisms driving the regional biophysical effects of LULCC on surface temperature, we use an energy balance decomposition approach. Following (Ge et al., 2021; Luyssaert et al., 2014; Winckler et al., 2017), this approach separates the surface temperature response to LULCC into contributions from individual terms of the surface energy balance (SEB) as follows:

$$\mathrm{DSR}\,(1-\alpha)+\mathrm{DLR}-\mathrm{LWup}=\mathrm{SH}+\mathrm{LH}+G \quad (1)$$

DSR represents downward shortwave radiation, DLR and LWup are downward and upward longwave radiations, SH and LH denote sensible and latent heat fluxes, and G is the ground heat flux (mainly soil heat storage), all in

Wm^2. Surface albedo (α) is the upward-to-downward shortwave radiation ratio. Using the Stefan–Boltzmann law, LWup can be rewritten as follows:

$$\mathrm{LWup} = \varepsilon\sigma T_s^4 \tag{2}$$

where σ is the Stefan–Boltzmann constant (5.67×10^{-8} $Wm^{-2}K^{-4}$), ε is surface emissivity, and T_s is the surface temperature (K). By taking the first-order derivative and rearranging Equation 1, the surface temperature response to LULCC is represented as follows:

$$\Delta T_s = \frac{1}{4\varepsilon\sigma T_s^{\,3}}(\Delta\mathrm{DSR} - \alpha\Delta\mathrm{DSR} - \mathrm{DSR}\Delta\alpha + \Delta\mathrm{DLR} - \Delta\mathrm{SH} - \Delta\mathrm{LH} - \Delta G) \tag{3}$$

where Δ represents the change induced by LULCC. Since different forest types interact with the atmosphere differently, indirect effects on DSR, DLR, and G are not neglected. To explore LULCC-induced changes in plant transpiration, soil evaporation, and canopy evaporation, the latent heat flux (LH), proportional to total evapotranspiration, is decomposed into the individual contributions from the terms in Equation 4 below:

$$\Delta\mathrm{LH} = \mathrm{Hvap}(\Delta\mathrm{Et} + \Delta\mathrm{Es} + \Delta\mathrm{Ec}) \tag{4}$$

where Hvap is the latent heat of vapourization (2.260 kJ/kg), and Et, Es, and Ec represent plant transpiration, soil evaporation, and canopy evaporation (all in mm). Applying Equation 4 to Equation 3, the surface temperature response to LULCC can be rewritten as follows:

$$\Delta T_s\,[\,K\,] = \frac{1}{4\varepsilon\sigma T_s^{\,3}}((1-\alpha)\Delta\mathrm{DSR} - \mathrm{DSR}\Delta\alpha + \Delta\mathrm{DLR} - \Delta\mathrm{SH} - \Delta\mathrm{Et} - \Delta\mathrm{Es} - \Delta\mathrm{Ec} - \Delta G) \tag{5}$$

While the energy balance decomposition approach does not directly attribute changes to all surface properties, such as aerodynamic roughness (Davin & Noblet-Ducoudré, 2010; Li et al., 2016), it helps to understand the relative contributions of each individual component within the SEB (Equation 5). This provides insights into LULCC-induced changes in surface temperature and their influence on extreme temperatures determined by surface upward long-wave radiation (Luyssaert et al., 2014).

3. Results

3.1. Model Performance Evaluation

WRF-Hydro system has shown good performance in simulating regional climate characteristics, including temperature, precipitation, radiation, heat fluxes, and runoff within our model domain (see Mortey et al., 2024). However, this study extends the validation framework by incorporating LAI assessments in addition to precipitation and temperature. Figure 2a shows that precipitation is generally well represented, with the model showing good agreement for the regional daily mean, achieving a correlation coefficient of 0.7, a percentage bias (PBIAS) of −9.9%, and a root mean square error (RMSE) of 2.5 mm/day. The model performs particularly well in the western region, closely matching observed spatial patterns. However, it underestimates the rainfall pattern in eastern Burkina Faso and Ghana and slightly overestimates it in northwestern Burkina Faso. For temperature, the model captures overall daily temperature variations and shows a good performance with a correlation coefficient of 0.8, a spatial daily mean bias of 0.02°C, and an RMSE of 1.3°C (Figure 2b). Spatially, the model shows a cold bias of about −1.5°C in the northern regions of Burkina Faso and a warm bias of about 1.5°C in the southern parts of Ghana. Regarding the LAI, Figures 2c–2e compare the simulated LAI with the interpolated CGLS LAI time series for the period 2014–2022. The analysis examines three randomly selected representative pixels, each corresponding to a distinct land cover category: grassland (Figure 2c), evergreen forest (Figure 2d), and mixed forest (Figure 2e). Overall, the model generally captures the annual vegetation dynamics for all land cover categories. The best model performance is observed for the evergreen forests, with a correlation coefficient of up to 0.86, followed by mixed forest ($r = 0.84$) and grassland ($r = 0.71$). The simulated LAI's root mean squared error (RMSE) varies between 0.33 and 0.67 depending on the land cover category. However, there are some discrepancies in specific years, particularly in the magnitude of the maximum LAI values and the rate of decline

10.1029/2025EF006094

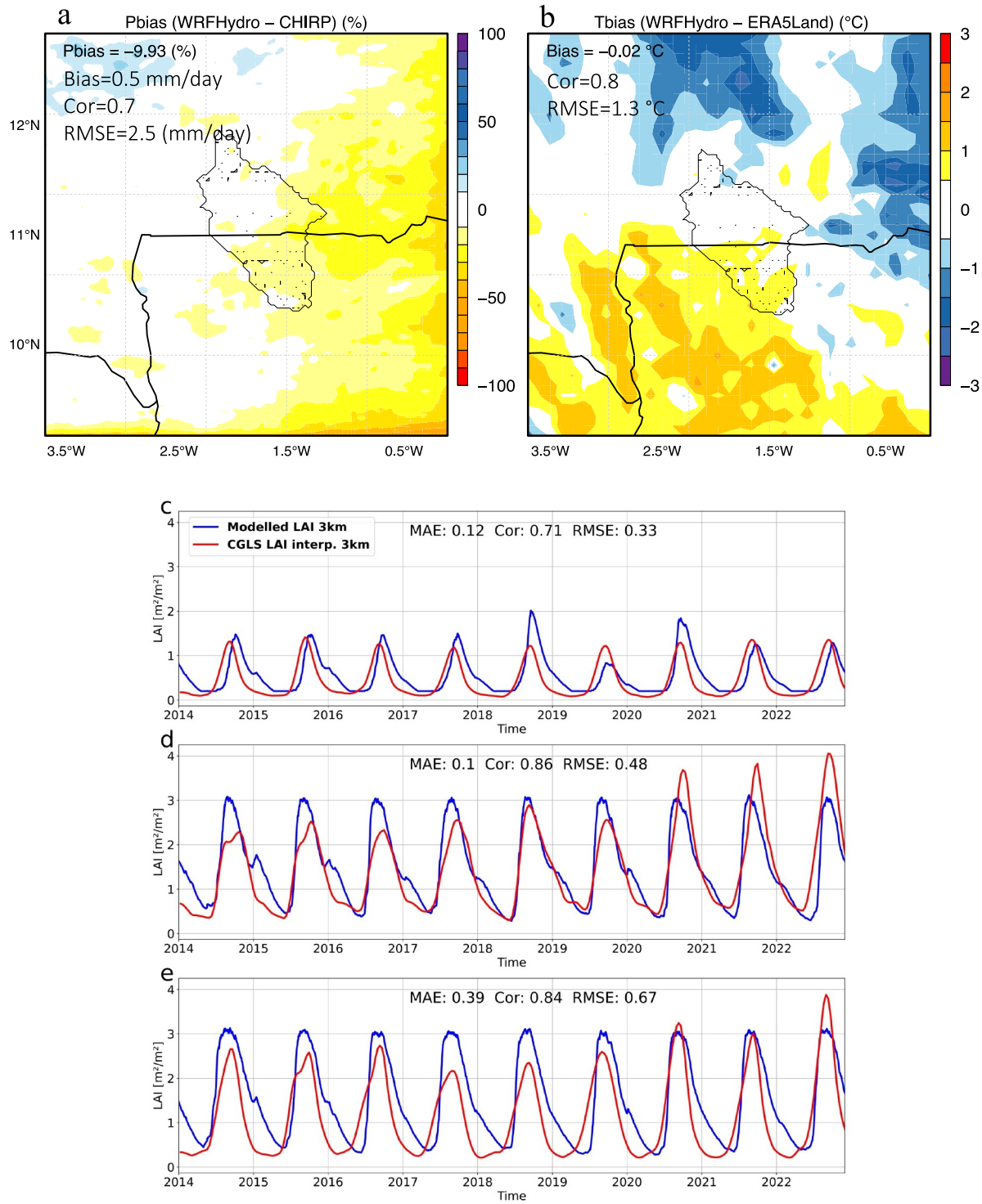

Figure 2. (a) Spatial patterns of the percentage bias (PBIAS, %) between simulated and observed daily mean precipitation for the period 2012–2022. (b) Spatial patterns of daily mean temperature bias (°C) between the simulated and observed daily mean temperature for the same period. (c), (d), and (e) compare the simulated leaf area index (LAI) with the interpolated Copernicus Land Monitoring Service LAI time series for 2014–2022. From January 2014 to June 2020, LAI data were derived from PROBA-V satellite observations (Smets et al., 2018), and from July 2020 onwards, Sentinel-3 Ocean and Land Color Instrument imagery was used (Fuster et al., 2020; Wolfs et al., 2022). The analysis focuses on three randomly representative selected pixels corresponding to different land cover categories: grassland (c), evergreen broadleaf forest (d), and mixed forest (e). The skill metrics, including regional mean PBIAS (%), spatial mean biases, Kendall rank correlations, and root mean square error (RMSE) values, are summarized in the upper left panel.

10.1029/2025EF006094

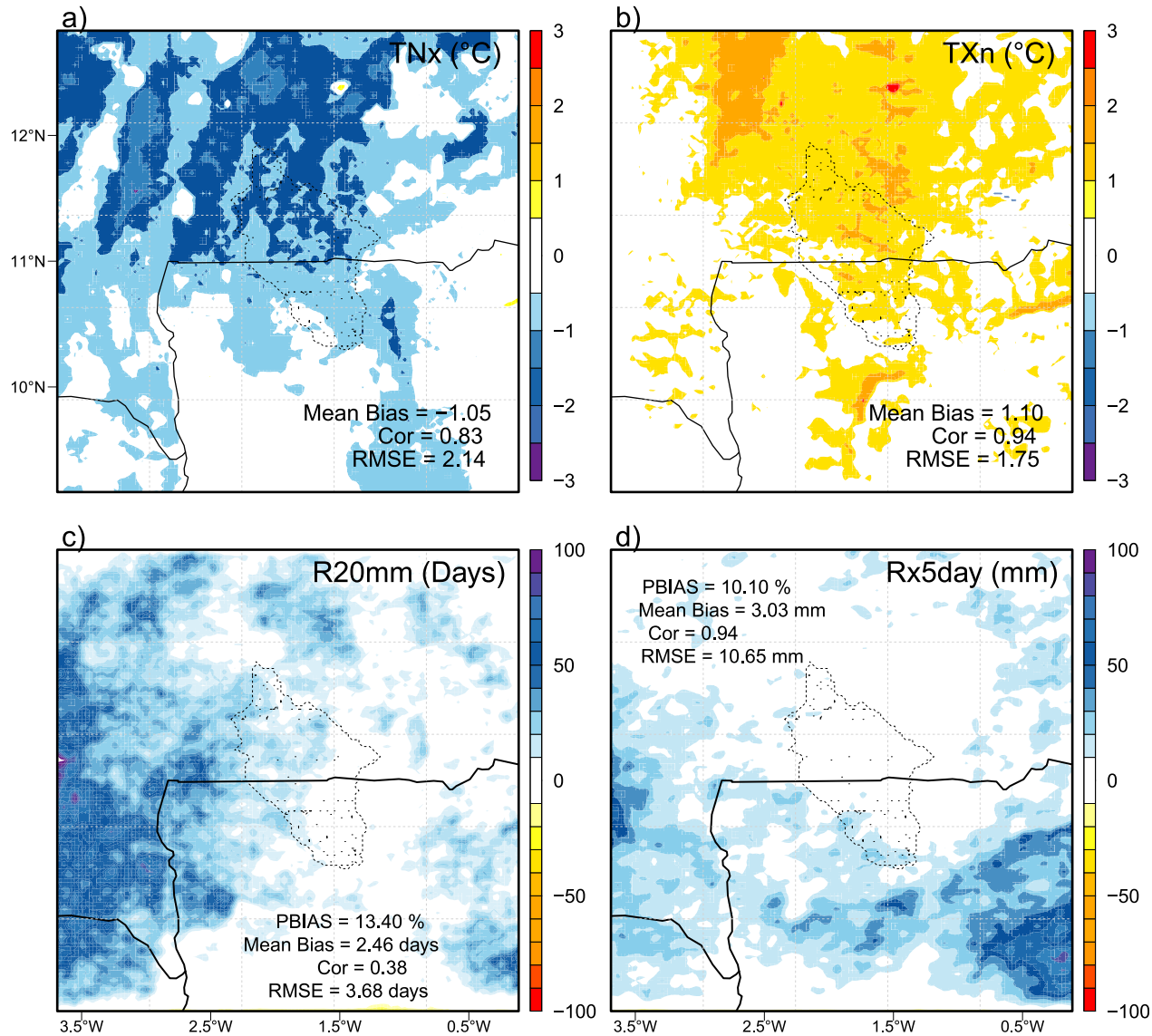

Figure 3. The model's ability to reproduce temperature and precipitation extremes over the period 2012–2022 is evaluated against ERA5-Land for temperature indices and CHIRPv2 for precipitation indices. (a) Spatial distribution of bias (°C), root mean square error (RMSE, °C), and Kendall's rank correlation coefficient (*r*) for TNx (monthly maximum of daily minimum temperatures); (b) the same set of metrics for TXn (monthly minimum of daily maximum temperatures); (c) spatial distribution of percentage bias (PBIAS, %), RMSE (mm), and correlation coefficient (*r*) for R20mm, representing the frequency of very heavy rainfall days (≥20 mm); and (d) spatial distribution of PBIAS (%), mean bias (mm), RMSE (mm), and correlation coefficient (*r*) for Rx5day, representing the maximum 5-day cumulative precipitation. Further performance metrics for the remaining extreme temperature and precipitation indices are provided in Tables S3 and S4 in Supporting Information S1.

after the seasonal peak during the growing season (July–October). Compared to satellite-derived LAI, the model tends to simulate a slower decline in LAI for grassland (Figure 2c) and mixed forest (Figure 2e). In addition, the model produces a secondary smaller peak in LAI across all land use categories for certain years, a feature not present in the CGLS data sets.

The performance of the model was also investigated, particularly in terms of extreme temperature and rainfall indices. Figure 3 shows that the model closely matches the observed spatial distribution of cold and hot temperature extremes, particularly in northern Ghana. However, performance varies between minimum and maximum temperature indices. For cold extremes (TNn and TNx; see Figure 3a and Table S3 in Supporting Information S1), the model exhibits a systematic cold bias, with a mean deviation of approximately −1.05°C relative to the observations, with the most pronounced bias observed in southern Burkina Faso. Despite this bias, the model captures the temporal variability of minimum temperatures well, achieving a high correlation

coefficient of $r = 0.83$. The associated root mean square error (RMSE) of 2.13°C indicates moderate deviation from the observed values. In contrast, for hot extremes (TXx and TXn; Figure 3b; Table S3 in Supporting Information S1), the model shows a positive mean bias of +1.10°C, suggesting a consistent overestimation of maximum daytime temperatures, particularly in southern Burkina Faso. Nevertheless, in this case, model performance improves, with a higher correlation coefficient ($r = 0.94$) and a lower RMSE of 1.75°C, indicating improved temporal agreement relative to the minimum temperature indices. Overall, these results highlight the model's ability to capture the spatial patterns and temporal dynamics of temperature extremes. However, it systematically underestimates cold extremes and overestimates hot extremes.

With regard to rainfall extremes, Figures 3c and 3d show that the model also closely matches the spatial distribution of precipitation indices, with particularly good agreement in southwestern Burkina Faso and northern Ghana. However, its performance differs notably between daily and multi-day rainfall indices (R20mm vs. Rx5day, see also Table S4 in Supporting Information S1). For R20mm, representing the number of days with very heavy rainfall (≥20 mm), the model shows a positive percentage bias (PBIAS) of 13.40% and a mean bias of +2.46 days. This suggests an overestimation of the frequency of intense daily rainfall events. Although the correlation coefficient is positive ($r = 0.38$), it is relatively low, suggesting that the model only partially captures the observed spatiotemporal variability of such events. The root mean square error (RMSE) of 3.68 days reflects moderate discrepancies, which are likely linked to the difficulty of accurately representing sub-daily convective processes that drive short-duration extreme rainfall. In contrast, the model performs considerably better for Rx5day, which captures the maximum cumulative precipitation over five consecutive days. Here, the model shows a smaller positive bias (PBIAS = 10.10%, mean bias = +3.03 mm), which is consistent with the R20mm results. However, it exhibits much stronger temporal agreement, with a high correlation coefficient ($r = 0.94$). The higher RMSE of 10.65 mm is expected due to the larger magnitude of the cumulative values. This better performance in simulating Rx5day indicates that the model more accurately captures the dynamics of longer-duration rainfall events (e.g., those associated with synoptic-scale systems or prolonged convection) than it does short-lived, high-intensity precipitation events.

While the model exhibits systematic biases—such as the underestimation of minimum temperatures, overestimation of maximum temperatures, and varying degrees of error in simulating precipitation extremes—these biases are not expected to affect the core conclusions of this study. This is because the analysis primarily emphasizes relative changes between land-use scenarios (e.g., deforestation vs. afforestation) rather than the absolute accuracy of the simulated climate variables.

3.2. Regional Contribution of Deforestation to Extreme Weather

The spatial patterns of changes in weather extremes, corresponding to a selection of the most significantly impacted temperature and precipitation extreme indices (six indices each) in response to deforestation, are shown in Figure 4 (see Table S2 in Supporting Information S1 for a full description of the extreme weather indices). Panel (a) displays the changes in mean and extreme temperature indices, while panel (b) depicts changes in mean and extreme precipitation indices. Deforestation induces a biophysical warming response across most temperature extreme indices. This warming is particularly pronounced—up to 2.0°C for Tmean—in the highly deforested areas of the south of Burkina Faso. However, an exception is observed for the daily maximum temperature indices (TXn and TXx), which show a slight cooling effect in parts of southeastern Burkina Faso. Despite this localized cooling, these indices still exhibit a warming response over the most heavily deforested zones (see Figure S6 in Supporting Information S1 for TXx patterns). Overall, the spatial patterns of extreme temperature indices closely resemble those of mean air temperature (Tmean) as well as those of surface (skin) temperature (hereinafter Tsurf; not shown), with significant spatial correlations (p-value < 0.05) observed for most of the temperature indices (Corr (Tmean; Textreme indices) > 0.82; Corr (Tsurf; Textreme indices) >0.62; see Table 2), except for the cold extreme indices (TXn, CSDI) and warm spell dry index (WSDI). At the seasonal scale, the deforestation-induced warming effect is more pronounced in winter (DJF) and autumn (SON), resulting in a significant increase in the minimum temperature of winter days and nights by up to 3.4 ± 0.27°C (refer to Figures S1–S4 in Supporting Information S1). Concerning rainfall extremes, the spatial patterns of extreme indices also closely resemble those of Pmean, exhibiting significant spatial correlations (p-value < 0.05) (Corr (Pmean; Pextreme indices) >0.86; see Table 2). The impacts of deforestation are also relatively pronounced, leading to a reduction in annual total precipitation on wet days (PRCPTOT, in mm), with average decreases of −23.89 ± 0.70 mm, and a more substantial decline in the number of wet days (R1mm, in days), averaging −3.0 ± 0.04 days. This drying trend is

10.1029/2025EF006094

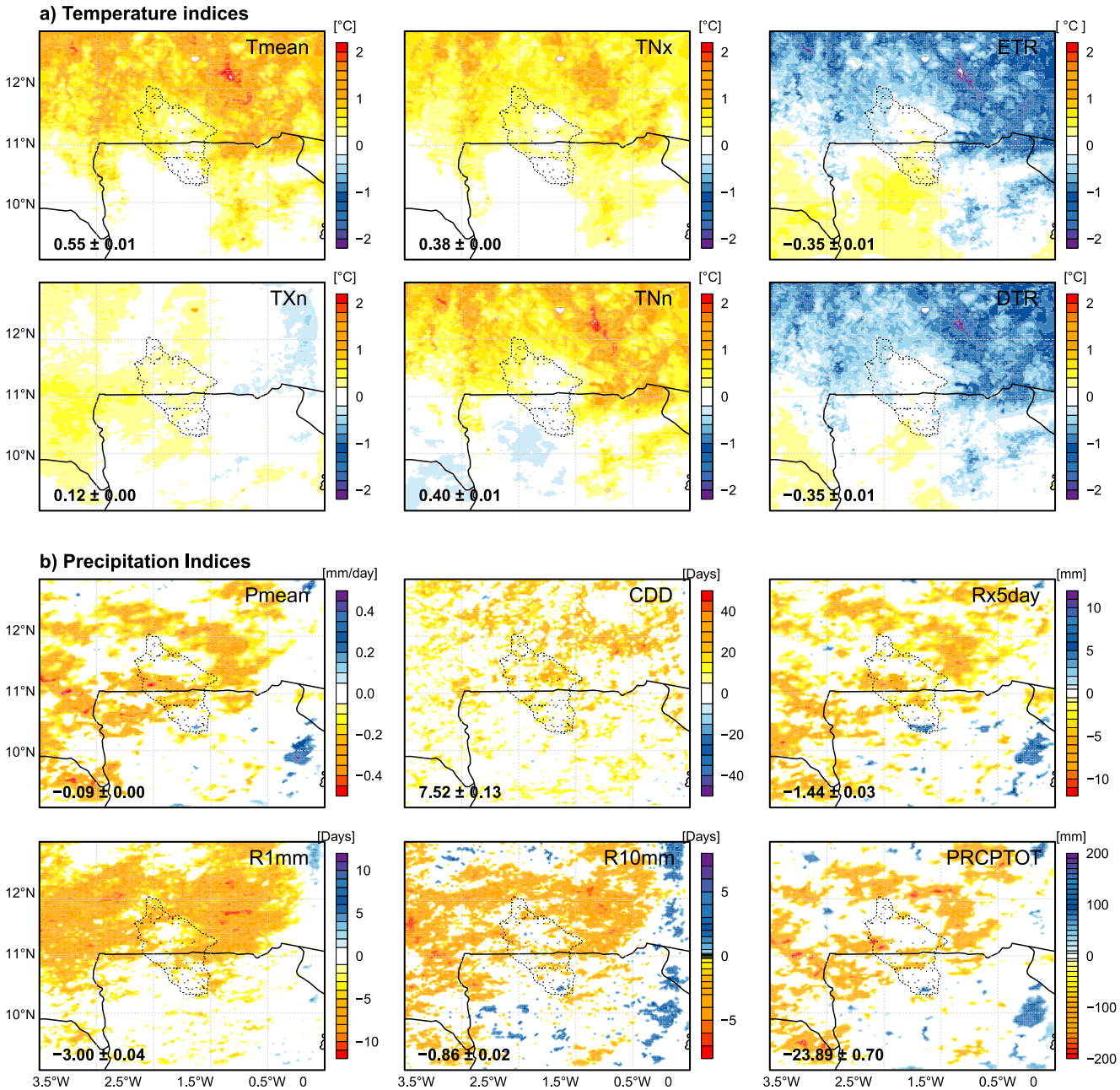

Figure 4. Spatial patterns of changes in temperature (a) and precipitation (b) indices in response to the deforestation experiment (CTL-NoLCC), averaged over the period 2012–2022, are shown. Mean and extreme weather indices are indicated in the top right of each panel (refer to the Methods section for details on extreme weather indices). Only grid points where changes are statistically significant at the 0.05 level using the Mann–Whitney–Wilcoxon (MWW) rank test are displayed (white/blank otherwise). The annual regionally averaged values and associated standard errors, calculated using Student's *t*-test at the 95% confidence level, are shown in the bottom-left corner of each panel. Only a sample of the most impacted temperature and precipitation extreme indices (six indices each) is shown. Figure S6 in Supporting Information S1 corresponds to spatial patterns of changes of the less impacted extreme temperature (TXx, CSDI, WSDI) and precipitation (R20mm, R95p, R99p, CWD, Rx1day) indices.

further accompanied by a significant increase in the number of consecutive dry days (CDD), reaching up to +7.52 ± 0.13 days. In analogy to extreme temperature, the spatial patterns of rainfall extremes are not uniform, especially for the heavy and extremely heavy rainfall day indices (R10mm and R20mm), demonstrating slightly different patterns from Pmean in the eastern part of Burkina Faso. However, they mimic the Pmean pattern above the highly deforested area in the southwest of Burkina Faso and the northeast of Ghana.

Table 2
Annual Kendall Rank Spatial Correlation Between Changes in Mean Air Temperature (Tmean), Surface Skin Temperature (Tsurf), and Pmean, and Their Respective Extreme Temperature and Precipitation Indices Under the Deforestation Scenario

Temperature indices			Precipitation indices	
Index	Corr (Tmean; Textreme indices)	Corr (Tsurf; Textreme indices)	Index	Corr (Pmean; Pextreme indices)
TXx	−0.38**	−0.17	Rx1day	0.46***
TNx	0.80***	0.62***	Rx5day	0.62***
TXn	−0.12*	0.03	R95p	0.36**
TNn	0.82***	0.55***	R99p	0.16*
DTR	−0.79***	−0.50***	R1mm	0.50***
ETR	−0.75***	−0.48***	R10mm	0.51***
WSDI	0.06	0.04	R20mm	0.56***
CSDI	−0.04	−0.14	CWD	0.11
Tmean		0.58***	PRCPTOT	0.86***
			CDD	−0.32**

Note. Star symbols are added to indicate significance: *** for p-value < 0.01, ** for p-value < 0.05, and * for p-value < 0.1. Refer to the Methods section for details on extreme weather indices.

The regional averaged contribution of deforestation to changes in mean and extreme weather indices is also presented in Figure 5. Accounting for the deforestation effect, we find a significant impact on both mean and extreme temperature indices, with the exception of WSDI and CSDI (expressed in days), where changes remain statistically insignificant. Notably, deforestation has a more pronounced impact on Tmean than on extreme temperatures. On average, deforestation results in a significant increase in mean temperature, reaching up to 0.55 ± 0.01°C. Additionally, it leads to an increase in the minimum temperature of winter days and nights, with TNn rising by 0.40 ± 0.01°C and TNx by 0.38 ± 0.01°C. Simultaneously, deforestation contributes to a reduction in DTR, with the difference between the climatological hottest day in spring and the coldest day in summer decreasing by −0.38 ± 0.04°C. Similarly, the extreme temperature range also declines by −0.4 ± 0.04°C. This reduction is primarily driven by a more rapid increase in daily minimum temperatures compared to daily maximum temperatures, as observed in the differential response of TXx and TXn versus TNn and TNx (see Figure 5, upper panel).

Conversely, deforestation has a more pronounced effect on some precipitation extremes compared to the mean precipitation condition (see Figure 5, bottom panel). Specifically, deforestation significantly reduces the regional mean precipitation (Pmean) by approximately −4.0% (0.09 ± 0.00 mm/day), the number of wet days (daily precipitation >1 mm; R1mm in days) by 7.0% (−3.0 ± 0.04 days), the frequency of rainy days (Rx1day in mm) by 3.0% (−0.8 ± 0.17 mm), the heavy precipitation days (R10mm in days) by 5.0% (−0.86 ± 0.02 days), and the total precipitation amount on wet days (PRCPTOT in mm) by 4.5% (−23.86 ± 0.7 mm) (see Figure 4 and Figure S14 in Supporting Information S1 for absolute contributions). Moreover, deforestation also contributes to reducing the very heavy precipitation days (R20mm in days) by 3.0% (−0.5 ± 0.11 days) and decreases the annual maximum consecutive 5-day precipitation (Rx5day in days) by 4.2% (−1.5 ± 0.25 days) leading to significant increase in consecutive dry days (CDD in days) by 5.5% (+7.52 ± 0.13 days). Overall, our results suggest that deforestation may impact some regional rainfall extremes (e.g., R1mm, R10mm, and PRCPTOT) more than the mean condition (Pmean) (see Figure 5).

3.3. Regional Contribution of Afforestation to Extreme Weather

Figure 6 shows the spatial patterns of changes in temperature and precipitation indices in response to the evergreen broadleaf forest-based afforestation scenario. For extreme temperature indices, a biophysical cooling effect is evident across the aforested regions. This cooling is particularly pronounced in southeastern Burkina Faso, where afforestation leads to substantial reductions in both mean and extreme temperature events. On average, afforestation results in a significant decrease in mean surface air temperature (Tmean) of up to −0.43 ± 0.01°C. Likewise, reductions are observed in cold and hot temperature extremes, with TNn and TNx decreasing by

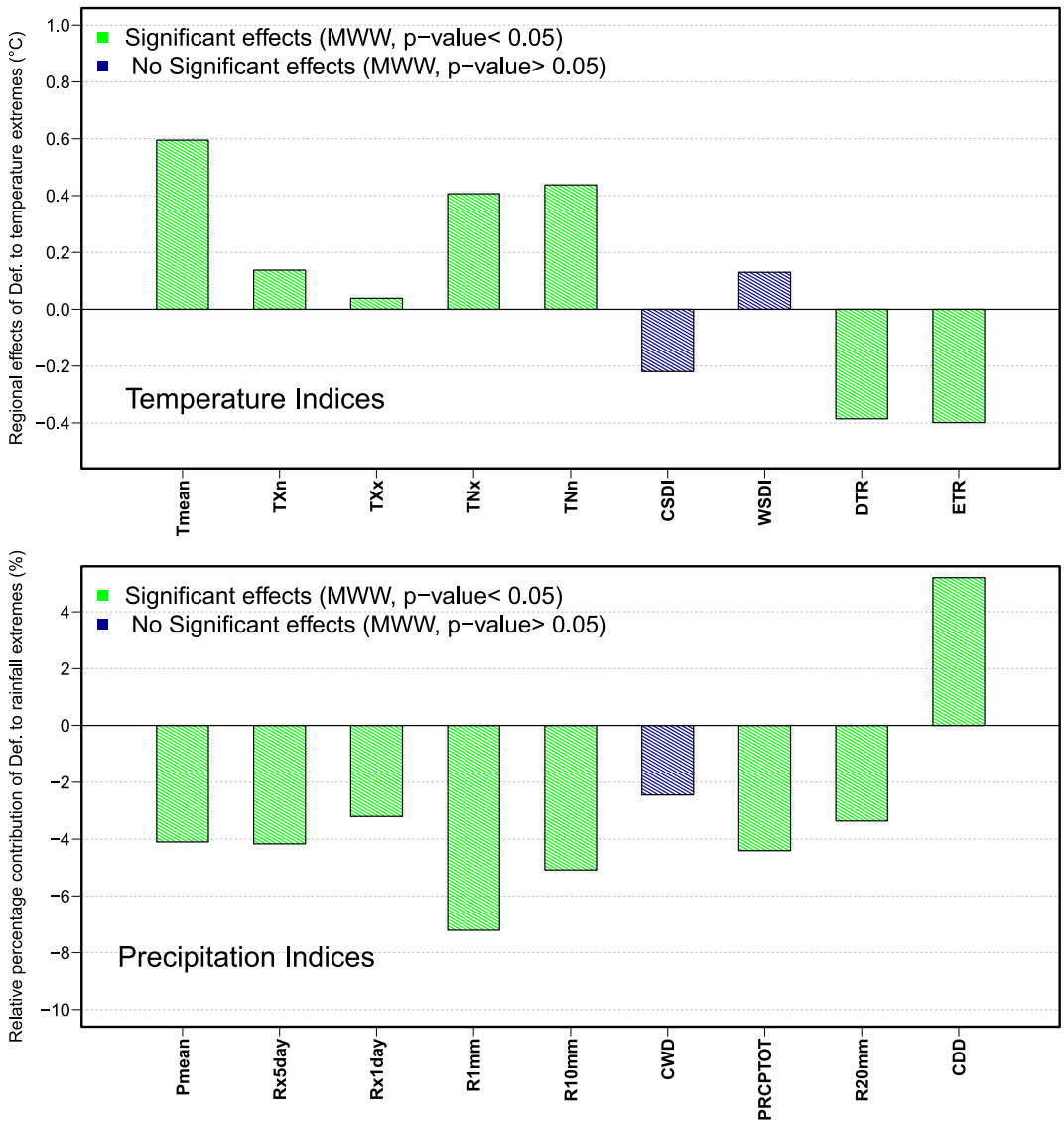

Figure 5. Regional averaged contribution of deforestation to mean and extreme weather indices (averaged over 2012–2022). The bars (*y*-axis) represent the absolute contribution of deforestation, calculated as (CTL–NoLCC), to the eight most affected temperature indices (°C) (top panel, *x*-axis). In the lower panel, the bars indicate the relative percentage contribution of deforestation (%) compared to the CTL simulation, calculated as (CTL–NoLCC)/CTL, for the eight most affected precipitation indices (*x*-axis). Green bars denote statistically significant changes based on the Mann–Whitney–Wilcoxon (MWW) test at the 0.05 level ($p < 0.05$), while blue bars represent indices where changes are not statistically significant ($p > 0.05$). All temperature extreme indices are expressed in °C, except for the Warm Spell Duration Index (WSDI) and Cold Spell Duration Index, which are expressed in days.

−0.32 ± 0.01°C and −0.27 ± 0.00°C, respectively, and TXn decreasing by −0.08 ± 0.00°C (Figure 6a). In terms of rainfall extremes (see Figure 6b), afforestation produces a clear hydrological response, with increases in both mean and extreme precipitation over the afforested zones. Notably, mean precipitation (Pmean) increases by 0.09 ± 0.00 mm/day, accompanied by a significant reduction in CDD by −6.67 ± 0.13 days, indicating a mitigation of drought conditions. Spatial patterns for the savanna, woody savanna, and mixed forest-based afforestation scenarios are provided in Figures S7–S9 in Supporting Information S1.

Figure 7 illustrates the regional averaged annual contributions of afforestation experiments to changes in a selection of the most negatively impacted temperature and precipitation indices (*y*-axis; seven indices each, as referenced in Figure 5) across different vegetation transition scenarios (*x*-axis). Regarding temperature extremes

10.1029/2025EF006094

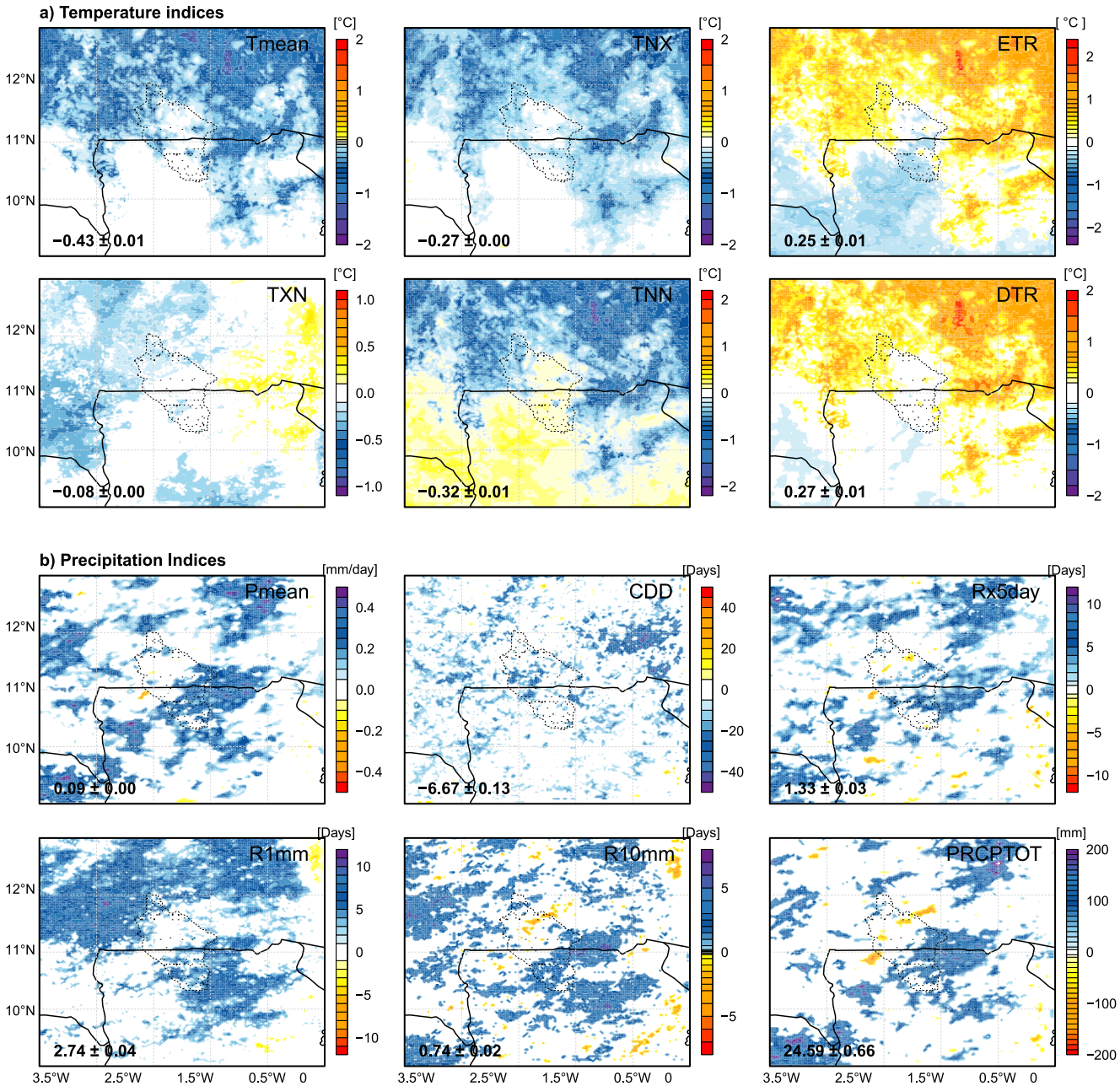

Figure 6. Similar to Figure 4, but for the spatial patterns of changes in temperature (a) and precipitation (b) indices in response to the mixed forest-based afforestation scenario ($AFF_{GRA/MIX}$–NoLCC). Mean and extreme weather indices are indicated in the top right corner of each panel. Only grid points with statistically significant changes ($p < 0.05$), based on the Mann–Whitney–Wilcoxon (MWW) rank test, are displayed; all others are left blank. The annual regionally averaged values and associated standard errors, calculated using Student's *t*-test at the 95% confidence level, are shown in the bottom-left corner of each panel. The black dashed contour in each panel outlines the Sissili River basin (Arnault et al., 2016). For clarity, only a subset of the most impacted temperature and precipitation extreme indices (six each) is presented. Figure S7–S9 in Supporting Information S1 corresponds to spatial patterns of changes in temperature (a) and precipitation (b) indices in response to evergreen/savannah/woody savannah-based forest-based afforestation scenarios.

(see Figure 7a), with the exception of the annual hottest days (TXx and TXn), afforestation scenarios involving the conversion of grassland to mixed forest ($AFF_{GRA/MXF}$) or evergreen forest ($AFF_{GRA/EBF}$) tend to mitigate the biophysical warming effect and reduce extreme temperature events. Specifically, these afforestation scenarios result in temperature reductions of up to −0.48 ± 0.02°C for Tmean, −0.35 ± 0.03°C for the annual coldest night (TNn in °C) and −0.3 ± 0.05°C for the annual coldest day (TNx in °C) (see also Figure S5 and S14 in Supporting Information S1 for the regional contribution of afforestation to mean and extreme weather indices). In other

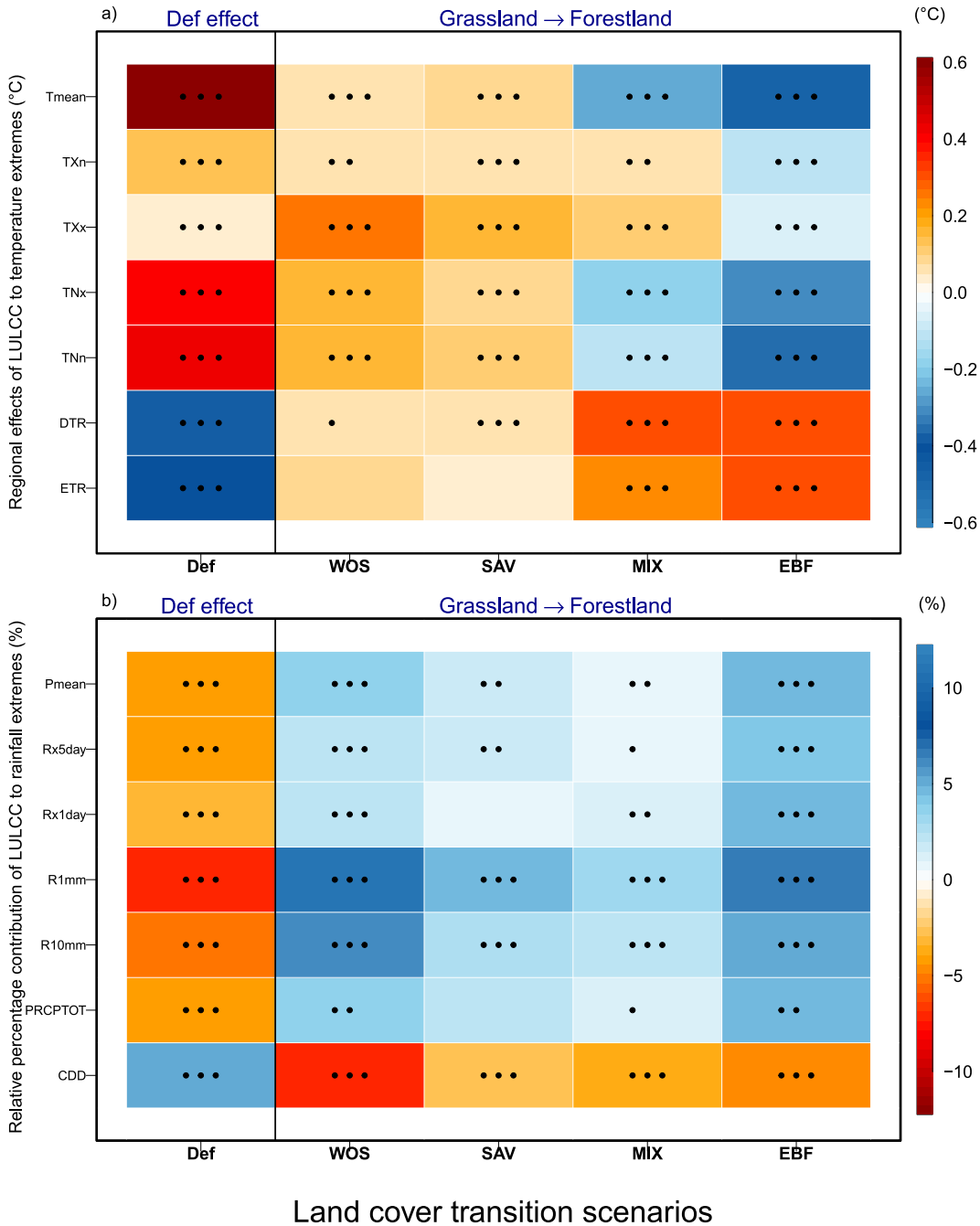

Figure 7. Regional contribution of deforestation and afforestation (*x*-axis) to changes in mean and extreme weather indices, averaged over 2012–2022. (a) The upper and lower mosaics depict the absolute contributions (°C) of deforestation and afforestation to the six most significantly affected temperature indices (top panel, *x*-axis). These contributions are computed as the difference between CTL and NoLCC for deforestation (Def) and between $AFF_{X/Y}$ and CTL for afforestation scenarios. (b) The upper and lower mosaics illustrate the relative percentage contributions (%) of deforestation and afforestation to the six most significantly affected precipitation extreme indices. The relative contribution of deforestation is assessed against the CTL simulation as (CTL–NoLCC)/CTL, whereas for afforestation, it is computed as ($AFF_{X/Y}$–CTL)/CTL. Here, $AFF_{X/Y}$ represents afforestation scenarios in which grassland (GRA) is converted into different forest types, including woody savanna (WOS), savanna (SAV), mixed forest (MXF), and evergreen forest (EBF). Positive (negative) values indicate warming (cooling) effects for temperature indices, while for precipitation, positive (negative) values correspond to wetter (drier) conditions. Statistically significant changes, determined by the Mann–Whitney–Wilcoxon (MWW) test, are indicated by black dots: one dot for $p < 0.1$, two dots for $p < 0.05$, and three dots for $p < 0.01$.

words, the cooling effects associated with the $AFF_{GRA/MXF}$ and $AFF_{GRA/EBF}$ experiments tend to offset the warming induced by deforestation, albeit to a lesser extent (see Figures S7 to S9 in Supporting Information S1 for the spatial patterns of changes in extreme temperature indices in response to all afforestation experiments). Conversely, the $AFF_{GRA/WOS}$ and $AFF_{GRA/SAV}$ experiments (i.e., conversion of grassland to woody savanna or savanna) show an opposite trend, contributing to an increase in all extreme temperature indices. In particular, $AFF_{GRA/WOS}$ and $AFF_{GRA/SAV}$ could lead to warming effects and increase hot temperature extremes (Figure 7a, Figure S7 in Supporting Information S1, and Table 3). This warming is attributed to the significant reduction of the surface albedo, which leads to increased absorption of solar radiation by the surface after afforestation (with values up to 1.09 ± 0.09°C for $AFF_{GRA/WOS}$ and up to 0.39 ± 0.03°C for $AFF_{GRA/SAV}$) (see Table 3). The most pronounced effects occur during the dry and hot season (from December to April), with values reaching up to 1.30 ± 0.10°C for $AFF_{GRA/WOS}$ in winter (see Table 3). Moreover, in the $AFF_{GRA/MXF}$, $AFF_{GRA/WOS}$, and $AFF_{GRA/SAV}$ scenarios, there is a notable increase in TXx and TXn, which aligns with the expanded vegetated area from afforestation. In other terms, the increase in maximum temperature extremes (TXx and TXn) from afforestation is typically mainly attributed to the reduction in surface albedo and the increase in relative humidity, which absorbs more solar radiation during the day (low albedo) while releasing less heat during the night (high humidity). Regarding precipitation extremes, the afforestation scenarios show a more uniform and consistent effect compared to the effect on temperature extremes (see Figure 7b). In other words, all afforestation experiments showed similar trends, leading to significant increases in both mean and extreme precipitation indices. In particular, the $AFF_{GRA/EBF}$ and $AFF_{GRA/WOS}$ scenarios resulted in increases of up to 10% in the number of wet days (R1mm) and heavy rainfall days (R10mm). In contrast, the effects of $AFF_{GRA/MXF}$ and $AFF_{GRA/SAV}$ were relatively small for most extreme precipitation indices (see Figure 7b and Figure S5 in Supporting Information S1). In terms of CDDs, all afforestation scenarios correspond to a shortening of droughts between 2.5% and 5% in the $AFF_{GRA/SAV}$, $AFF_{GRA/MXF}$, $AFF_{GRA/EBF}$ scenarios, and up to 7% in the $AFF_{GRA/WOS}$ experiment.

3.4. Potential Mechanisms Driving the Contrasting Responses to Temperature Extremes

To further investigate the underlying physical mechanisms driving the contrasting extreme temperature responses to different vegetation transition scenarios, Figure 8 illustrates the changes in surface temperature attributed to different components of the SEB (see Equation 5). These include changes in downward shortwave radiation (ΔDSR), downward longwave radiation (ΔDLR), surface albedo ($\Delta\alpha$), sensible heat flux (ΔSH), plant transpiration (ΔEt), canopy evaporation (ΔEc), soil evaporation (ΔEs) and ground heat flux (ΔG), as described in Equation 5 (see Methods section for details). Regarding deforestation (Figure 8a), surface temperature responses are influenced by various compensating phenomena (see also Table 4). These include local physical mechanisms such as changes driven by albedo-induced cooling effects (up to -0.87 ± 0.06°C; see Table 4 and Figure 8a) versus total evapotranspiration-induced warming effects (up to 1.22 ± 0.18°C; refer to Figures 8a, Figure S10 in Supporting Information S1, and Table 4). Although evapotranspiration contributes significantly to warming throughout the year, the impact of albedo-induced cooling is more evident during the dry winter months (DJF), when evaporative fluxes are limited. Under these conditions, the temperature response associated with albedo can locally reach -1.15 ± 0.08°C (see Table 4), which partially offsets the warming effect. Conversely, the temperature response driven by evapotranspiration, primarily influenced by the reduction in plant transpiration, dominates during the post-monsoon (SON) season (with values up to 3.4 ± 0.27°C; see Table 4). Consequently, winter days and nights, corresponding to the minimum values of daily maximum temperature (TXn; see Figure 8a), tend to experience cooling due to deforestation-induced increases in surface albedo (see Figure S10 in Supporting Information S1). This seasonal dynamic explains why minimum daily maximum temperatures (TXn; Figure 8a), typically occurring in winter, tend to cool due to albedo-driven effects, while the highest temperature extremes (TXx and TNx; Figures S7 and S9 in Supporting Information S1), which occur in spring and fall, show a pronounced warming signal linked to reduced evapotranspiration (see Figure 9 and Figure S10 in Supporting Information S1). On average, this trend coincides with the simulated signals for extreme annual temperature indices (Figures 4 and 5, upper panels) and at seasonal scales (see Figures S1 and S4 in Supporting Information S1).

Regarding afforestation, $AFF_{GRA/MXF}$ and $AFF_{GRA/EBF}$ (see Figures 8d and 8e) demonstrate significant biophysical cooling effects for almost throughout the year, with a more pronounced signal (up to -0.47 ± 0.02°C and -0.26 ± 0.01°C, on average, respectively, see Figures S5 and S14 in Supporting Information S1) during the dry and hot periods (i.e., from October to May, corresponding to the pre- or post-monsoonal periods) primarily driven

Table 3

Annual and Seasonal Mean Values of Biophysical Effects of all Afforestation Experiments ($AFF_{GRA/EBF}$, $AFF_{GRA/MXF}$, $AFF_{GRA/WOS}$ and $AFF_{GRA/SAV}$) on Surface Temperature (°C) Attributed to Changes in Downward Shortwave Radiation (ΔDSR), Downward Longwave Radiation (ΔDLR), Surface Albedo (Δα), Sensible Heat Flux (ΔSH), Plant Transpiration (ΔEt), Canopy Evaporation (ΔEc), Soil Evaporation (ΔEs), and Ground Heat Flux (ΔG), as Outlined in Equation 5 (Refer to the Methods Section for Details)

	Annual				DJF				MAM			
SEB (°C)	EBF	MXF	WOS	SAV	EBF	MXF	WOS	SAV	EBF	MXF	WOS	SAV
ΔTs	**−0.87 ± 0.08**	**−0.60 ± 0.06**	0.04 ± 0.03	0.05 ± 0.01	**−0.93 ± 0.09**	**−0.40 ± 0.05**	**0.45 ± 0.03**	**0.24 ± 0.01**	**−0.82 ± 0.06**	**−0.63 ± 0.05**	0.09 ± 0.03	0.00 ± 0.01
ΔDSR	**−0.43 ± 0.02**	**−0.30 ± 0.02**	**−0.51 ± 0.03**	**−0.19 ± 0.01**	**−0.14 ± 0.003**	−0.07 ± 0.00	**−0.10 ± 0.00**	**−0.02 ± 0.00**	**−0.51 ± 0.02**	**−0.410.01**	**−0.42 ± 0.01**	**−0.15 ± 0.01**
ΔDLR	**0.57 ± 0.03**	**0.36 ± 0.01**	**0.79 ± 0.02**	**0.21 ± 0.00**	**0.79 ± 0.02**	**0.48 ± 0.00**	**0.85 ± 0.01**	**0.22 ± 0.003**	**0.85 ± 0.03**	**0.50 ± 0.02**	**0.42 ± 0.02**	**0.20 ± 0.00**
Δα	**0.75 ± 0.06**	**0.48 ± 0.04**	**1.09 ± 0.09**	**0.39 ± 0.03**	**0.98 ± 0.08**	**0.57 ± 0.04**	**1.30 ± 0.10**	**0.42 ± 0.03**	**0.90 ± 0.06**	**0.45 ± 0.03**	**0.80 ± 0.05**	**0.25 ± 0.01**
ΔSH	**−0.32 ± 0.07**	**−0.50 ± 0.06**	**−0.56 ± 0.09**	**−0.25 ± 0.04**	**−0.23 ± 0.04**	**−0.77 ± 0.06**	**−0.46 ± 0.03**	**−0.25 ± 0.02**	**−0.44 ± 0.08**	**−0.49 ± 0.07**	−0.08 ± 0.05	−0.04 ± 0.03
ΔG	0.01 ± 0.00	0.01 ± 0.00	−0.01 ± 0.00	−0.00 ± 0.00	−0.08 ± 0.00	−0.03 ± 0.00	−0.09 ± 0.00	−0.02 ± 0.001	0.05 ± 0.006	0.02 ± 0.00	0.03 ± 0.004	0.01 ± 0.003
ΔEt	**−2.05 ± 0.20**	**−0.82 ± 0.09**	**−0.81 ± 0.08**	**−0.10 ± 0.02**	**−1.87 ± 0.16**	**−0.44 ± 0.04**	**−0.60 ± 0.04**	**−0.06 ± 0.007**	**−0.75 ± 0.06**	**−0.20 ± 0.02**	**−0.20 ± 0.01**	−0.01 ± 0.00
ΔEs	**1.00 ± 0.19**	**0.37 ± .09**	**0.51 ± 0.14**	0.06 ± 0.05	**−0.12 ± 0.01**	−0.01 ± 0.00	−0.14 ± 0.02	−0.02 ± 0.005	**−0.43 ± 0.06**	**−0.32 ± 0.04**	**−0.45 ± 0.04**	**−0.25 ± 0.04**
ΔEc	−0.11 ± 0.01	−0.04 ± 0.00	−0.08 ± 0.01	−0.02 ± 0.00	0.00 ± 0.00	−0.00 ± 0.00	−0.00 ± 0.00	0.00 ± 0.00	−0.07 ± 0.007	−0.02 ± 0.00	−0.03 ± 0.00	0.00 ± 0.00
R	−0.01 ± 0.00	−0.01 ± 0.00	−0.03 ± 0.00	−0.01 ± 0.00	0.00 ± 0.00	−0.00 ± 0.00	−0.00 ± 0.00	0.00 ± 0.00	−0.02 ± 0.00	−0.01 ± 0.00	−0.02 ± 0.003	0.00 ± 0.00

Note. ΔTs denotes the calculated net change in surface temperature (derived from the radiation budget) induced by afforestation, which is approximately the sum of the terms on the right-hand side of Equation 5. *R* accounts for the residual term (calculated as the difference between the terms on the left-hand and right-hand sides of Equation 5), illustrating the closure of the surface energy balance (SEB). Changes that are statistically significant at the 95% confidence interval (CI) - as determined by the Wilcoxon-Mann-Whitney test at the 0.05 significance level - are highlighted in bold. Positive values (in red) indicate warming effects, while negative values (in blue) indicate cooling effects. Uncertainty estimates are expressed as standard errors, calculated using the Student's *t*-test at the 95% confidence level.

by increased plant transpiration. In other words, in $AFF_{GRA/MXF}$ and $AFF_{GRA/EBF}$, cold temperature extremes are influenced by various afforestation-induced compensating physical phenomena. These include: (a) the local forest transpiration, which remains highly predominant throughout the year due to the substantial increase in foliar density, and (b) the decrease in soil evaporation during the monsoon period (JJAS), reducing the cooling effects driven by plant transpiration. This means that a significant reduction in soil evaporation is only partially offset by a lesser increase in plant transpiration, thereby reducing the latent heat flux during the monsoon period (see Table 3). These dynamics can be interpreted by various physical mechanisms at play: during the pre- or post-monsoonal periods, more incoming radiation (in line with less cloud cover) is transferred to the atmosphere by an increase in turbulent heat flux, particularly in latent heat flux (as a result of increased plant transpiration due to the enhanced canopy foliage), leading to a significant decrease in heat extreme events (Figures 8d and 8e). Conversely, during the monsoon period, the warmer and wetter climate conditions, along with increased solar radiation, tend to promote tree/vegetation growth, resulting in a reduction in soil evaporation due to the increased canopy foliage, which reduces soil exposure to the incoming shortwave radiation and surface wind speed.

By contrast, $AFF_{GRA/WOS}$ and $AFF_{GRA/SAV}$ experiments (refer to Figures 8d and 8e) demonstrate a warming effect for almost the entire year (up to 0.07 ± 0.00°C and 0.08 ± 0.01°C, on average, respectively, see Figures S5 and S14 in Supporting Information S1), with a greater magnitude observed during the pre- or post-monsoonal periods. In other words, in $AFF_{GRA/WOS}$ and $AFF_{GRA/SAV}$ experiments, hot temperature extremes are influenced by various afforestation-induced compensating factors across different seasons (see Figures 8d and 8e). During the pre- or post-monsoonal periods, the hot temperature extremes are primarily influenced by the albedo-induced warming effect (values reaching up to 1.55 ± 0.12°C for $AFF_{GRA/WOS}$ and 0.67 ± 0.05°C for $AFF_{GRA/SAV}$ in SON; see Figures 8d and 8e and Table 3), which results in increased absorption of shortwave radiation at the surface. During the monsoon period, the albedo-driven temperature response is amplified by reduced soil evaporation, albeit slightly countered by a minor increase in forest transpiration and sensible heat flux associated with the increase in canopy foliage.

3.5. Potential Mechanisms Driving the Changes in Extreme Precipitation

Figure 9 shows the spatial patterns of changes in precipitation and evapotranspiration during the West African Monsoon (WAM) season (June–September, JJAS). This provides further insight into the physical mechanisms that cause changes in extreme precipitation in response to different LCC scenarios. Evapotranspiration plays a fundamental role in modulating WAM dynamics through land–atmosphere interactions. However, it is important to acknowledge that this study does not analyze total vertically integrated moisture flux convergence, an essential process that influences mid-tropospheric convection, due to the lack of vertical atmospheric data in the WRF-Hydro model outputs. In the deforestation scenario, as shown in Figure 9a, close spatial coherence is observed

JJA				SON			
EBF	MXF	WOS	SAV	EBF	MXF	WOS	SAV
−0.54 ± 0.05	**−0.54 ± 0.05**	−0.11 ± 0.02	0.07 ± 0.01	**−1.20 ± 0.09**	**−0.83 ± 0.06**	**−0.29 ± 0.04**	−0.10 ± 0.02
−0.69 ± 0.03	**−0.44 ± 0.03**	**−0.76 ± 0.03**	**−0.26 ± 0.02**	**−0.38 ± 0.02**	**−0.30 ± 0.01**	**−0.75 ± 0.02**	**−0.33 ± 0.01**
0.42 ± 003	**0.22 ± 0.02**	**0.24 ± 0.02**	**0.09 ± 0.00**	**0.24 ± 0.01**	**0.25 ± 0.01**	**0.57 ± 0.02**	**0.31 ± 0.01**
0.32 ± 0.02	**0.23 ± 0.02**	**0.72 ± 0.06**	**0.23 ± 0.02**	**0.8 ± 0.06**	**0.66 ± 0.05**	**1.55 ± 0.12**	**0.67 ± 0.05**
−0.66 ± 0.09	**−0.34 ± 0.05**	**−0.57 ± 0.10**	**−0.19 ± 0.04**	0.01 ± 0.06	**−0.40 ± 0.05**	**−1.11 ± 0.14**	**−0.52 ± 0.07**
−0.03 ± 0.00	0.00 ± 0.00	−0.04 ± 0.005	−0.02 ± 0.00	0.12 ± 0.012	0.06 ± 0.01	0.04 ± 0.009	0.01 ± 0.00
−2.39 ± 0.22	**−1.43 ± 0.14**	**−1.31 ± 0.12**	**−0.11 ± 0.02**	**−3.17 ± 0.27**	**−1.20 ± 0.10**	**−1.11 ± 0.09**	**−0.24 ± 0.03**
3.17 ± 0.28	**1.58 ± 0.14**	**1.98 ± 0.21**	**0.42 ± 0.05**	**1.41 ± 0.19**	**0.24 ± 0.06**	**0.65 ± 0.16**	0.09 ± 0.06
−0.27 ± 0.02	−0.11 ± 0.01	−0.17 ± 0.01	−0.02 ± 0.00	−0.10 ± 0.01	−0.04 ± 0.00	−0.12 ± 0.01	−0.05 ± 0.00
−0.02 ± 0.00	−0.01 ± 0.00	−0.04 ± 0.004	−0.01 ± 0.00	−0.02 ± 0.002	−0.01 ± 0.00	−0.04 ± 0.00	−0.01 ± 0.00

between reductions in precipitation and evapotranspiration, particularly in heavily deforested regions such as southern Burkina Faso. This pattern suggests that local land–atmosphere feedback, mainly driven by reduced evapotranspiration, substantially modulates precipitation responses, exhibiting significant spatial correlations ($r = 0.4$; p-value < 0.05, not shown), indicating strong coupling. In other terms, deforestation leads to surface drying, with average reductions in evapotranspiration reaching 0.01 mm/day. This decline in moisture recycling likely reduces latent heat fluxes and near-surface humidity, thereby potentially inhibiting boundary layer development and constraining the northward progression of the monsoon front. Consequently, regional precipitation is significantly altered, with observed decreases in both mean and extreme rainfall (see Figure 3). By contrast, the afforestation experiments (Figures 9b and 9c) consistently exhibit increases in both evapotranspiration and precipitation, underscoring the critical role of vegetation density in modulating land–atmosphere interactions. Close spatial patterns between enhanced evapotranspiration and increased precipitation are evident across forested areas in the southern Burkina Faso. The strongest hydrological responses are observed in the $AFF_{GRA/EBF}$ scenario, where evapotranspiration increases by up to approximately 0.009 mm/day, compared to about 0.005 mm/day in the $AFF_{GRA/WOS}$ scenario. These increases are likely driven by enhanced latent heat fluxes, which support deeper and more organized convection. As a result, afforestation contributes to greater mean and extreme precipitation, fewer dry days, and reduced drought durations (see Figures 6 and 7).

4. Discussion

This study offers a novel perspective on the biophysical impacts of deforestation and afforestation scenarios on regional climate extremes in the West African savanna region. It achieves this through two primary approaches: firstly, by conducting high-resolution LULCC experiments at a 3 km resolution, thereby capturing the fine-scale effects associated with various ecosystem transition scenarios; and secondly, by employing an advanced fully coupled atmosphere-hydrology model system (i.e., WRF-Hydro; see Arnault et al., 2023; Mortey et al., 2024; Ndiaye et al., 2024). This study is the first to use the advanced WRF-Hydro system over West Africa to assess regional climate extremes in response to vegetation perturbations, incorporating both dynamic vegetation feedback and terrestrial hydrological processes—features often omitted in earlier studies (e.g., Camara et al., 2022; Diba et al., 2018; Ingrosso & Pausata, 2024). While previous work has focused mainly on the drier Sahel using single regional or global climate models (e.g., Abiodun et al., 2013; Diba et al., 2018; Ingrosso & Pausata, 2024; Odoulami et al., 2019), our approach provides a more integrated assessment. Furthermore, as afforestation is one of the main land-based mitigation strategies proposed in scenarios consistent with the Paris Agreement goals (Grassi et al., 2017; Griscom et al., 2017; Harper et al., 2018), it is important to evaluate its broader impacts beyond CO_2 mitigation.

10.1029/2025EF006094

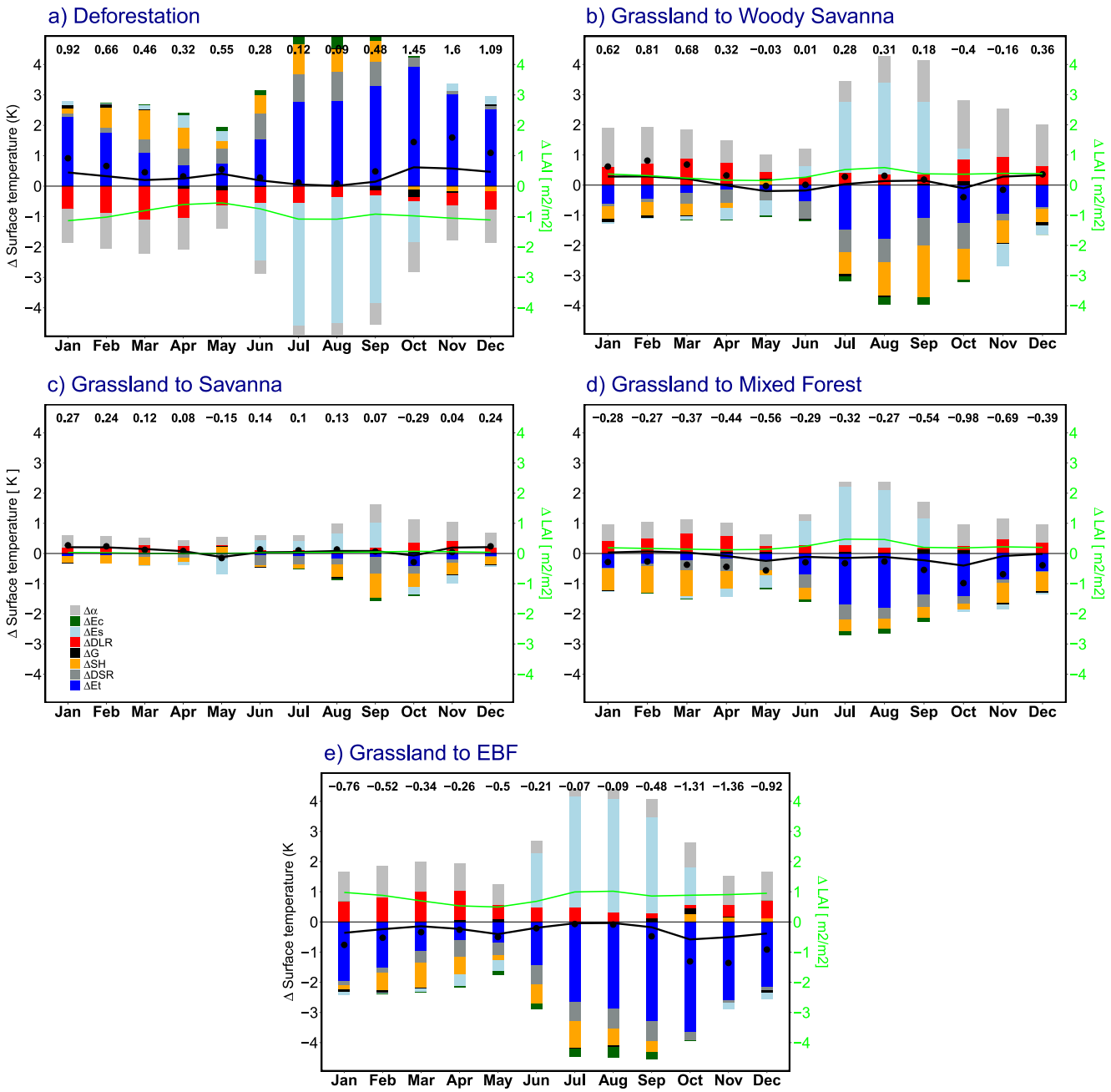

Figure 8. Surface energy balance decomposition of monthly mean surface temperature changes (K) in response to deforestation and afforestation experiments. The stacked bars represent surface temperature changes (K) due to contributions from changes in downward shortwave radiation (ΔDSR in dark gray), downward longwave radiation (ΔDLR in red), surface albedo (Δα in light gray), sensible heat flux (ΔSH in yellow), plant transpiration (ΔEt in blue), canopy evaporation (ΔEc in dark green), soil evaporation (ΔEs in light blue), and ground heat flux (ΔG in black), as outlined in Equation 5 (refer to Methods section for details). The black lines depict the net change in surface air temperature (Tmean), while the black dots and the values shown at the top of each bar represent the calculated net change in surface temperature (derived from the radiation budget) caused by deforestation (a) and by afforestation scenarios (b, c, d, e), which approximately corresponds to the sum of the bars in the respective month. The green lines represent changes in the leaf area index (ΔLAI), illustrating changes in canopy leaf density.

Our study shows that deforestation leads to a simulated biophysical warming response (up to 0.55 ± 0.01°C, on average), with the most pronounced signals over the highly deforested area in southwestern Burkina Faso and northeastern Ghana. These results are consistent with previous studies based on observational data (Duveiller et al., 2018b, 2020) and modeling experiments (e.g., Butt et al., 2023; Cohn et al., 2019; Davin & Noblet-Ducoudré, 2010; Jia et al., 2019; Mahmood et al., 2014; Perugini et al., 2017; Sy & Quesada, 2020), which have

Table 4

Similar to Table 3 for the Annual and Seasonal Mean Values of the Regional Biophysical Effects of Deforestation on Surface Temperature (°C) Attributed to Changes in Downward Shortwave Radiation (ΔDSR), Downward Longwave Radiation (ΔDLR), Surface Albedo (Δα), Sensible Heat Flux (ΔSH), Plant Transpiration (ΔEt), Canopy Evaporation (ΔEc), Soil Evaporation (ΔEs), and Ground Heat Flux (ΔG), as Outlined in Equation 5 (Refer to the Methods Section for Details)

SEB component contributions (°C)	Annual	DJF	MAM	JJA	SON
ΔTs	0.97 ± 0.08	1.12 ± 0.09	0.91 ± 0.06	0.54 ± 0.05	1.30 ± 0.10
ΔDSR	0.55 ± 0.03	0.15 ± 0.01	0.57 ± 0.01	1.00 ± 0.04	0.45 ± 0.02
ΔDLR	−0.62 ± 0.03	−0.83 ± 0.02	−0.90 ± 0.03	−0.48 ± 0.03	−0.27 ± 0.01
Δα	−0.87 ± 0.06	−1.15 ± 0.08	−1.01 ± 0.06	−0.36 ± 0.02	−0.95 ± 0.07
ΔSH	0.41 ± 0.08	0.26 ± 0.05	0.53 ± 0.08	0.74 ± 0.10	0.12 ± 0.08
ΔG	−0.02 ± 0.01	0.09 ± 0.00	−0.06 ± 0.00	0.01 ± 0.00	−0.14 ± 0.01
ΔEt	2.20 ± 0.20	2.16 ± 0.17	0.84 ± 0.06	2.41 ± 0.21	3.40 ± 0.27
ΔEs	−1.10 ± 0.19	0.15 ± 0.01	0.45 ± 0.06	−3.47 ± 0.27	−1.55 ± 0.20
ΔEc	0.12 ± 0.01	0.00 ± 0.00	0.07 ± 0.00	0.31 ± 0.02	0.12 ± 0.01
R	−0.02 ± 0.00	−0.01 ± 0.00	−0.03 ± 0.00	−0.03 ± 0.00	−0.03 ± 0.00

Note. Changes that are statistically significant at the 95% confidence interval (CI) - as determined by the Wilcoxon-Mann-Whitney test at the 0.05 significance level - are highlighted in bold.

consistently shown that deforestation in tropical regions induces significant biophysical warming effects. Perugini et al. (2017), incorporating a broader range of tropical subregional studies, identified a comparable and significant biophysical warming effect of 0.60 ± 0.74°C across tropical zones (based on $n = 34$ simulations from 12 studies). Despite using coarse-resolution simulations, Boone et al. (2016) reported similar warming effects in West Africa, although the magnitude of warming varied considerably between different climate models. Our study demonstrates that the most pronounced warming effects observed during the pre- and post-monsoon seasons are also evident in changes in temperature extremes, with a more significant impact on winter days and night minimum temperatures (TNn, TNx) (see Figure 4a). These results are consistent with previous research that has identified a particularly significant response of temperature extremes to deforestation (e.g., Abera et al., 2024; Findell et al., 2017; Hirsch et al., 2018; Lejeune et al., 2018; Sy & Quesada, 2020). However, extreme temperature responses (both cold and hot extremes) are influenced by various compensating phenomena induced by deforestation (see Figure 8a). These include (a) local physical mechanisms such as changes driven by albedo-induced cooling effects versus evapotranspiration-induced warming effects (refer to Figures 8a, Figure S10 in Supporting Information S1, and Table 4), (b) regional responses (e.g., local deforestation compared to LULCC in other regions), and (c) local effects confined to deforested grid cells versus non-local effects which may occur in both deforested and non-deforested areas (e.g., Chen et al., 2022; Winckler et al., 2017). On the other hand, our study also demonstrates that, on average, deforestation can significantly reduce regional extreme rainfall by 7% (−3.2 ± 0.24 days) for the number of wet days (daily precipitation>1 mm; R1mm) and by 5% (−1.2 ± 0.15 days) for heavy rainfall days (daily precipitation>10 mm; R10mm) more than the mean rainfall conditions (Pmean) (see Figures 4 and 5), also leading to an intensification of the number of dry days (precipitation <1 mm) and increase drought lengths by (+7.52 ± 0.13 days). Such findings are also consistent with some previous research indicating that deforestation can affect rainfall extremes more profoundly than mean rainfall conditions (e.g., Sy & Quesada, 2020), and particularly in monsoonal regions like West Africa (Quesada et al., 2017). The responses of extreme rainfall to deforestation are also predominantly driven by changes in evapotranspiration (see Figure 9 and Figure S10 in Supporting Information S1), which lead to a reduction in local moisture supply to the WAM monsoon system. This can be interpreted by various mechanisms at play: on average, deforestation reduces shallower vegetation and foliar density, leading to a large decrease in evapotranspiration during the monsoon season (Figure 9a and Figure S10 in Supporting Information S1), which results in less interception of surface water and reduced soil moisture, ultimately leading to lower mean and extreme precipitation. This pattern is consistent with findings from numerous studies (Mahmood et al., 2014; Perugini et al., 2017; Sy & Quesada, 2020). Soil moisture depletion can intensify temperature extremes due to its non-linear interaction with the temperature distribution, which extends beyond the mean response (Pall et al., 2007; Seneviratne et al., 2010). While changes in mean precipitation under warming are primarily driven by energy availability, extreme

10.1029/2025EF006094

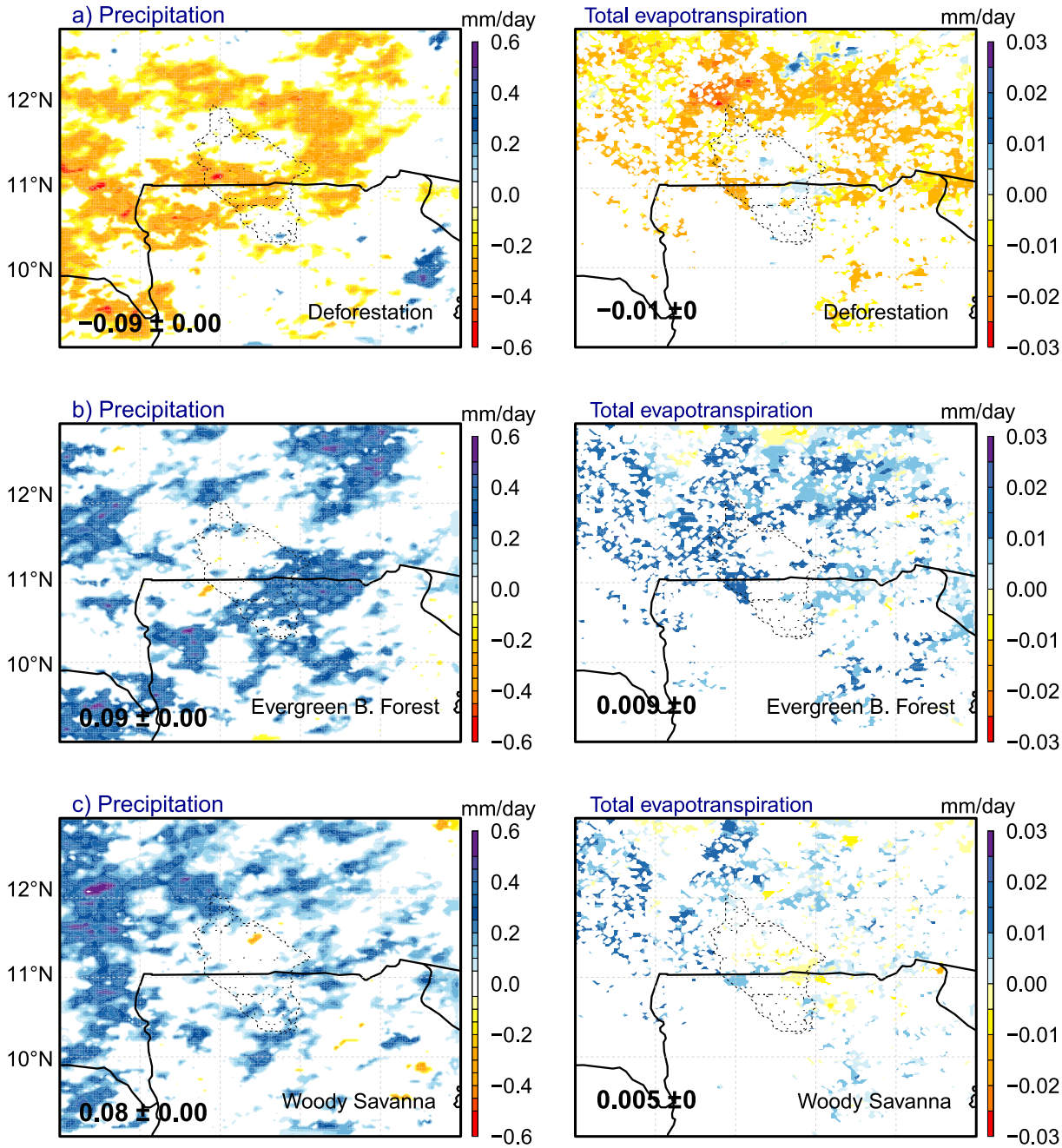

Figure 9. Spatial patterns of changes in precipitation (mm/day) and evapotranspiration (mm/day) in response to (a) deforestation and afforestation scenarios based on evergreen broadleaf forest (b) and woody savanna (c). Only grid points with statistically significant changes ($p < 0.05$), determined using the Mann–Whitney–Wilcoxon (MWW) rank test, are shown; non-significant areas are left blank. The regionally averaged values and associated standard errors, calculated using Student's *t*-test at the 95% confidence level, are shown in the bottom-left corner of each panel. For clarity, only a subset of the most impacted afforestation scenarios is displayed (see Figure 7). Figure S11 in Supporting Information S1 corresponds to the changes in precipitation (mm/day) and evapotranspiration (mm/day) in response to afforestation scenarios based on mixed forest and savanna.

precipitation is more strongly influenced by near-surface moisture levels, exhibiting approximately three times greater sensitivity to temperature changes (Pall et al., 2007). Deforestation can amplify these effects by (a) reducing atmospheric moisture through decreased leaf density and transpiration and (b) increasing surface albedo, which causes surface cooling and weakens precipitation processes, aligning with the Clausius-Clapeyron relationship (IPCC-SRCCL, 2019). As a result, deforestation is expected to suppress extreme precipitation events to a greater extent than mean precipitation levels.

Regarding afforestation, our results highlight contrasting biophysical responses of temperature extremes to different afforestation scenarios. Conversion of grassland to evergreen or mixed forest mitigates the biophysical warming effect and reduces extreme heat events, with the strongest cooling observed under the evergreen-based afforestation scenario (see Figures 6a, 8d, and 8e, and Figure S5 in Supporting Information S1). This cooling effect is likely driven by increased canopy foliage following afforestation, which enhances evapotranspiration (see Figure 9) and likely atmospheric moisture availability. The resulting rise in humidity can promote cloud formation (Abera et al., 2024; Teuling et al., 2017), thereby reducing incoming solar radiation and heat extremes. Conversely, afforestation with a transition from grassland to woody savanna or savanna is associated with more frequent extreme heat events, especially during the pre- and post-monsoon periods, mainly due to an albedo-induced warming effect (Figures 8b and 8c; Figures S7, S8, S12, and S14 in Supporting Information S1). This warming persists throughout the year and may be exacerbated by reduced soil evaporation during the monsoon season (Figures 8b and 8c; Table 3). In addition, all afforestation scenarios generally lead to an increase in mean and extreme precipitation, a decrease in dry days, and, consequently, a reduction in drought lengths (see Figure 7). These changes are primarily governed by local land–atmosphere feedbacks, particularly those linked to increased evapotranspiration and moisture availability (see Figure 9), which likely contribute to the northward expansion of the monsoon (Ingrosso & Pausata, 2024; Pausata et al., 2020). These results are also consistent with recent findings by Ingrosso and Pausata (2024) those who examined different afforestation scenarios with different forest densities and types under global warming projections in the Sahel. Their study revealed that, despite considerable increases in total moisture flux convergence under afforestation scenarios, changes in evapotranspiration remained the dominant driver of increased extreme rainfall, closely associated with forest type and density. They also concluded that while afforestation generally increases precipitation, it can also induce an albedo-driven warming effect, leading to more frequent extreme heat events during the pre-monsoon season.

Overall, our results highlight the importance of carefully considering multiple land cover transitions for afforestation, as biophysical variables show contrasting responses depending on vegetation type. For example, previous studies have shown that afforestation in West Africa often leads to cooling effects, especially during the monsoon season (Bamba et al., 2019; Camara et al., 2022; Diba et al., 2018). Our results are consistent with these findings, particularly for afforestation with evergreen or MXF, where increased plant transpiration contributes to reduced surface temperatures. However, when analyzing specific forest types, such as woody savanna and savanna, different responses emerge. Specifically, we also observe a greater increase in plant transpiration during transitions from grassland to evergreen forest compared to conversion from grassland to woody savanna. In other words, while woody savannas can have lower transpiration rates than evergreen forests due to reduced vegetation density, soil evaporation can compensate for this difference and may even dominate total evapotranspiration, especially during the monsoon season. Therefore, to fully understand the net impact of forest cover change - including afforestation and reforestation initiatives such as the GGW West Africa - it is essential to consider the specific nature of the transition and the associated biophysical effects. Overall, these afforestation experiments should be seen as idealized land use and land management change scenarios for the West African savanna region. By integrating forest and cropland ecosystems, they provide valuable insights into the multiple climate impacts of various afforestation-based land management strategies. Actions such as climate-smart agriculture can not only mitigate the effects of climate change but also promote the sustainable development of agriculture, forestry, and related industries (FOA-IPCC, 2017).

5. Limitations and Future Perspectives

While the idealized simulations conducted in this study, employing an advanced fully coupled atmosphere-hydrology modeling system (WRF-Hydro; Arnault et al., 2023; Mortey et al., 2024; Ndiaye et al., 2024), offer insights into the potential biophysical impacts of various LCC transition scenarios on weather extremes, it is important to note that these findings are derived from a single climate model and configuration. Although the WRF-Hydro model demonstrates strong performance in capturing vegetation dynamic, temperature, and precipitation patterns across our study area, future studies should employ additional models, particularly convection-permitting models (Yahaya Seydou et al., 2025). In other words, although our simulations are conducted using a scale-aware convective parameterization scheme (Grell & Freitas, 2014), which has shown significant improvement in the representation of heavy rainfall events (Park et al., 2022, 2024), some studies suggest that parameterized convection models may exhibit a response to the soil moisture-precipitation feedback that is different from, or even opposite to, that of convection-permitting models (Hohenegger et al., 2009; Taylor

et al., 2013). However, a recent study by Jungandreas et al. (2023) demonstrated that the monsoon circulation's response to enhanced vegetation cover over West Africa in a convection-permitting model is qualitatively similar to that in simulations with parameterized convection, though more pronounced. This amplified response is mainly driven by changes in soil moisture, which are significantly influenced by runoff dynamics and precipitation patterns. Further research utilizing both convection-permitting models and those with parameterized convection is necessary to quantify and constrain this response more accurately. This is critical because LULCC can also affect atmospheric dynamics such as cloud cover, cloud base height, diabatic processes within the PBL, and large-scale circulations, which in turn can indirectly affect climate extremes through atmospheric feedback mechanisms (e.g., Cao et al., 2023; Chen et al., 2022). These atmospheric effects can extend beyond the afforested/deforested areas, affecting neighboring regions (Abiodun et al., 2013; Ingrosso & Pausata, 2024) and even remote areas up to 100 km from the forest location (Butt et al., 2023; Cohn et al., 2019). Furthermore, our results depend on the model's ability to represent the complex structure of forest types, such as savannas, which may have a more complicated three-dimensional structure compared to evergreen or deciduous forests. This may oversimplify certain cooling mechanisms, such as increased surface roughness, which increases air mixing and contributes to cooling. It is important to note that while the transformation of grasslands into evergreen or MXF can contribute to the mitigation of global warming and extreme heat, this process may also result in groundwater depletion, particularly if the trees do not significantly change rainfall patterns. Addressing these complexities in future work could improve our understanding of the wider impacts of afforestation on regional climate extremes.

Finally, while recent observations indicate an increasing trend in vegetation greenness across large areas of the Sahel, likely driven by partial rainfall recovery (e.g., Herrmann et al., 2005; Jury, 2018), these potential changes were not considered in this study. Future research should consider the potential influence of ongoing greening, as this could either amplify or offset the future biophysical impacts of LCC on climate extremes.

6. Conclusions and Implications

At the regional level, our findings have crucial implications for climate and policy assessments and highlight the importance of considering the biophysical effects of afforestation and their impact on regional climate extremes in the West African Savannas region, consistent with prior research (Abiodun et al., 2013; Camara et al., 2022; Diba et al., 2018; Doelman et al., 2020; Ingrosso & Pausata, 2024; Odoulami et al., 2019). They contribute to enhancing the WAM (Ingrosso & Pausata, 2024) and may lead to increased extreme precipitation, contingent upon the types of forests planted, while also influencing temperature extremes differently. In summary, the international policy process under the United Nations Framework Convention on Climate Change exclusively addresses the biogeochemical impacts of afforestation on global radiative forcing (Mahmood et al., 2014; Perugini et al., 2017), which raises concerns about accurately communicating information regarding land-based climate mitigation. Consequently, we anticipate that this study will inspire further investigation into the comprehensive effects of the potential benefits and trade-offs associated with afforestation. This, in turn, will enhance the dissemination of robust and reliable messages regarding land management strategies within the context of climate-smart agriculture in the West African Savannas region.

Conflict of Interest

The authors declare no conflicts of interest relevant to this study.

Data Availability Statement

The WRF-Hydro model system used in this study is publicly available (Gochis et al., 2020). The model data supporting the results of this study are available in (Sy, 2025). The original Leaf Area Index (LAI) product is accessible via the CLMS platform (Copernicus, 2023).

Acknowledgments
This research is supported by the Federal Ministry of Education and Research of Germany (BMBF) through the West African Science Service Center on Climate Change and Adapted Land Use (WASCAL) and the Concerted Regional Modeling and Observation Assessment for Greenhouse Gas Emissions and Mitigation Options under Climate and Land Use Change in West Africa (CONCERT-West Africa; Grant 01LG2089A BMBF). The simulations were conducted on the Linux cluster at KIT/IMK-IFU in Garmisch-Partenkirchen. The authors would like to thank the two anonymous reviewers for their constructive feedback, which significantly improved the quality of the paper.

References

Abera, T. A., Heiskanen, J., Maeda, E. E., Muhammed, M. A., Bhandari, N., Vakkari, V., et al. (2024). Deforestation amplifies climate change effects on warming and cloud level rise in African montane forests. *Nature Communications*, *15*(1), 6992. https://doi.org/10.1038/s41467-024-51324-7

Abiodun, B. J., Pal, J. S., Afiesimama, E. A., Gutowski, W. J., & Adedoyin, A. (2008). Simulation of West African monsoon using RegCM3 part II: Impacts of deforestation and desertification. *Theoretical and Applied Climatology*, *93*(3), 245–261. https://doi.org/10.1007/s00704-007-0333-1

Abiodun, B. J., Salami, A. T., Matthew, O. J., & Odedokun, S. (2013). Potential impacts of afforestation on climate change and extreme events in Nigeria. *Climate Dynamics*, *41*(2), 277–293. https://doi.org/10.1007/s00382-012-1523-9

Achugbu, I. C., Laux, P., Olufayo, A. A., Balogun, I. A., Dudhia, J., Arnault, J., et al. (2023). The impacts of land use and land cover change on biophysical processes in West Africa using a regional climate model experimental approach. *International Journal of Climatology*, *43*(4), 1731–1755. https://doi.org/10.1002/joc.7943

Achugbu, I. C., Olufayo, A. A., Balogun, I. A., Adefisan, E. A., Dudhia, J., & Naabil, E. (2022). Modeling the spatiotemporal response of dew point temperature, air temperature and rainfall to land use land cover change over West Africa. *Modeling Earth Systems and Environment*, *8*(1), 173–198. https://doi.org/10.1007/s40808-021-01094-8

Arnault, J., Fersch, B., Rummler, T., Zhang, Z., Quenum, G. M., Wei, J., et al. (2021). Lateral terrestrial water flow contribution to summer precipitation at continental scale – A comparison between Europe and West Africa with WRF-Hydro-tag ensembles. *Hydrological Processes*, *35*(5), e14183. https://doi.org/10.1002/hyp.14183

Arnault, J., Mwanthi, A. M., Portele, T., Li, L., Rummler, T., Fersch, B., et al. (2023). Regional water cycle sensitivity to afforestation: Synthetic numerical experiments for tropical Africa. *Frontiers in Climate*, *5*, 1233536. https://doi.org/10.3389/fclim.2023.1233536

Arnault, J., Wagner, S., Rummler, T., Fersch, B., Bliefernicht, J., Andresen, S., & Kunstmann, H. (2016). Role of runoff–infiltration partitioning and resolved overland flow on land–atmosphere feedbacks: A case study with the WRF-hydro coupled modeling system for West Africa. *Journal of Hydrometeorology*, *17*(5), 1489–1516. https://doi.org/10.1175/JHM-D-15-0089.1

Arora, V. K., & Montenegro, A. (2011). Small temperature benefits provided by realistic afforestation efforts. *Nature Geoscience*, *4*(8), 514–518. https://doi.org/10.1038/ngeo1182

Bala, G., Caldeira, K., Wickett, M., Phillips, T. J., Lobell, D. B., Delire, C., & Mirin, A. (2007). Combined climate and carbon-cycle effects of large-scale deforestation. *Proceedings of the National Academy of Sciences*, *104*(16), 6550–6555. https://doi.org/10.1073/pnas.0608998104

Bamba, A., Diallo, I., Touré, N. E., Kouadio, K., Konaré, A., Dramé, M. S., et al. (2019). Effect of the African greenbelt position on West African summer climate: A regional climate modeling study. *Theoretical and Applied Climatology*, *137*(1), 309–322. https://doi.org/10.1007/s00704-018-2589-z

Bliefernicht, J., Berger, S., Salack, S., Guug, S., Hingerl, L., Heinzeller, D., et al. (2018). The WASCAL hydrometeorological observatory in the Sudan Savanna of Burkina Faso and Ghana. *Vadose Zone Journal*, *17*(1), 1–20. https://doi.org/10.2136/vzj2018.03.0065

Bonan, G. B. (2008). Forests and climate change: Forcings, feedbacks, and the climate benefits of forests. *Science*, *320*(5882), 1444–1449. https://doi.org/10.1126/science.1155121

Boone, A. A., Xue, Y., De Sales, F., Comer, R. E., Hagos, S., Mahanama, S., et al. (2016). The regional impact of land-use land-cover change (LULCC) over West Africa from an ensemble of global climate models under the auspices of the WAMME2 project. *Climate Dynamics*, *47*(11), 3547–3573. https://doi.org/10.1007/s00382-016-3252-y

Boysen, L. R., Brovkin, V., Pongratz, J., Lawrence, D. M., Lawrence, P., Vuichard, N., et al. (2020). Global climate response to idealized deforestation in CMIP6 models. *Biogeosciences*, *17*(22), 5615–5638. https://doi.org/10.5194/bg-17-5615-2020

Breil, M., Davin, E. L., & Rechid, D. (2021). What determines the sign of the evapotranspiration response to afforestation in European summer? *Biogeosciences*, *18*(4), 1499–1510. https://doi.org/10.5194/bg-18-1499-2021

Butt, E. W., Baker, J. C. A., Bezerra, F. G. S., von Randow, C., Aguiar, A. P. D., & Spracklen, D. V. (2023). Amazon deforestation causes strong regional warming. *Proceedings of the National Academy of Sciences*, *120*(45), e2309123120. https://doi.org/10.1073/pnas.2309123120

Camara, M., Diba, I., & Diedhiou, A. (2022). Effects of land cover changes on compound extremes over West Africa using the regional climate model RegCM4. *Atmosphere*, *13*(3), 421. https://doi.org/10.3390/atmos13030421

Cao, Y., Guo, W., Ge, J., Liu, Y., Chen, C., Luo, X., & Yang, L. (2023). Greening vegetation cools mean and extreme near-surface air temperature in China. *Environmental Research Letters*, *19*(1), 014040. https://doi.org/10.1088/1748-9326/ad122b

Chen, C., Ge, J., Guo, W., Cao, Y., Liu, Y., Luo, X., & Yang, L. (2022). The biophysical impacts of idealized afforestation on surface temperature in China: Local and nonlocal effects. *Journal of Climate*, *35*(23), 7833–7852. https://doi.org/10.1175/JCLI-D-22-0144.1

Cohn, A. S., Bhattarai, N., Campolo, J., Crompton, O., Dralle, D., Duncan, J., & Thompson, S. (2019). Forest loss in Brazil increases maximum temperatures within 50 km. *Environmental Research Letters*, *14*(8), 084047. https://doi.org/10.1088/1748-9326/ab31fb

Cook-Patton, S. C., Leavitt, S. M., Gibbs, D., Harris, N. L., Lister, K., Anderson-Teixeira, K. J., et al. (2020). Mapping carbon accumulation potential from global natural forest regrowth. *Nature*, *585*(7826), 545–550. https://doi.org/10.1038/s41586-020-2686-x

Copernicus. (2023). Leaf area index 2014-present (raster 300m), global, 10-daily - version 1.0 [Dataset]. *Copernicus Land Monitoring Service (CLMS)*. https://doi.org/10.2909/219fdc9f-616b-444b-a495-198f527b4722

Croux, C., & Dehon, C. (2010). Influence functions of the spearman and Kendall correlation measures. *Statistical Methods and Applications*, *19*(4), 497–515. https://doi.org/10.1007/s10260-010-0142-z

Davin, E. L., & de Noblet-Ducoudré, N. (2010). Climatic impact of global-scale deforestation: Radiative versus nonradiative processes. *Journal of Climate*, *23*(1), 97–112. https://doi.org/10.1175/2009JCLI3102.1

Davin, E. L., Rechid, D., Breil, M., Cardoso, R. M., Coppola, E., Hoffmann, P., et al. (2020). Biogeophysical impacts of forestation in Europe: First results from the LUCAS (land use and climate across scales) regional climate model intercomparison. *Earth System Dynamics*, *11*(1), 183–200. https://doi.org/10.5194/esd-11-183-2020

Deme, A., Gaye, A. T., & Hourdin, F. (2017). Chapter 3. Climate projections in West Africa: The obvious and the uncertain. In B. Sultan, R. Lalou, M. A. Sanni, A. Oumarou, & M. Arame Soumaré (Eds.), *Rural societies in the face of climatic and environmental changes in West Africa* (pp. 61–86). IRD Éditions. https://doi.org/10.4000/books.irdeditions.12325

Diba, I., Camara, M., & Diedhiou, A. (2018). Impacts of the Sahel-Sahara interface reforestation on West African climate: Intra-annual variability and extreme temperature events. *Atmospheric and Climate Sciences*, *9*(1), 35–61. https://doi.org/10.4236/acs.2019.91003

Diouf, I., Sy, S., Senghor, H., Fall, P., Diouf, D., Diakhaté, M., et al. (2022). Potential contribution of climate conditions on COVID-19 pandemic transmission over West and North African countries. *Atmosphere*, *13*(1), 34. https://doi.org/10.3390/atmos13010034

Doelman, J. C., Stehfest, E., van Vuuren, D. P., Tabeau, A., Hof, A. F., Braakhekke, M. C., et al. (2020). Afforestation for climate change mitigation: Potentials, risks and trade-offs. *Global Change Biology*, *26*(3), 1576–1591. https://doi.org/10.1111/gcb.14887

Duveiller, G., Caporaso, L., Abad-Viñas, R., Perugini, L., Grassi, G., Arneth, A., & Cescatti, A. (2020). Local biophysical effects of land use and land cover change: Towards an assessment tool for policy makers. *Land Use Policy*, *91*, 104382. https://doi.org/10.1016/j.landusepol.2019.104382

Duveiller, G., Hooker, J., & Cescatti, A. (2018a). A dataset mapping the potential biophysical effects of vegetation cover change. *Scientific Data*, *5*(1), 180014. https://doi.org/10.1038/sdata.2018.14

Duveiller, G., Hooker, J., & Cescatti, A. (2018b). The mark of vegetation change on Earth's surface energy balance. *Nature Communications*, *9*(1), 679. https://doi.org/10.1038/s41467-017-02810-8

Elagib, N. A., Khalifa, M., Babker, Z., Musa, A. A., & Fink, A. H. (2021). Demarcating the rainfed unproductive zones in the African Sahel and Great Green Wall regions. *Land Degradation & Development*, *32*(3), 1400–1411. https://doi.org/10.1002/ldr.3793

Fersch, B., Senatore, A., Adler, B., Arnault, J., Mauder, M., Schneider, K., et al. (2020). High-resolution fully coupled atmospheric–hydrological modeling: A cross-compartment regional water and energy cycle evaluation. *Hydrology and Earth System Sciences*, *24*(5), 2457–2481. https://doi.org/10.5194/hess-24-2457-2020

Findell, K. L., Berg, A., Gentine, P., Krasting, J. P., Lintner, B. R., Malyshev, S., et al. (2017). The impact of anthropogenic land use and land cover change on regional climate extremes. *Nature Communications*, *8*(1), 989. https://doi.org/10.1038/s41467-017-01038-w

FOA-IPCC. (2017). FAO-IPCC expert meeting on climate change, land use and food security: Final meeting report.

Funk, C., Peterson, P., Landsfeld, M., Pedreros, D., Verdin, J., Shukla, S., et al. (2015). The climate hazards infrared precipitation with stations—A new environmental record for monitoring extremes. *Scientific Data*, *2*(1), 150066. https://doi.org/10.1038/sdata.2015.66

Furnari, L., Magnusson, L., Mendicino, G., & Senatore, A. (2022). Fully coupled high-resolution medium-range forecasts: Evaluation of the hydrometeorological impact in an ensemble framework. *Hydrological Processes*, *36*(2), e14503. https://doi.org/10.1002/hyp.14503

Fuster, B., Sánchez-Zapero, J., Camacho, F., García-Santos, V., Verger, A., Lacaze, R., et al. (2020). Quality assessment of PROBA-V LAI, fAPAR and fCOVER collection 300 m products of Copernicus global land service. *Remote Sensing*, *12*(6), 1017. https://doi.org/10.3390/rs12061017

Ge, J., Qiu, B., Chu, B., Li, D., Jiang, L., Zhou, W., et al. (2021). Evaluation of coupled regional climate models in representing the local biophysical effects of afforestation over continental China. *Journal of Climate*, *34*(24), 9879–9898. https://doi.org/10.1175/JCLI-D-21-0462.1

Glotfelty, T., Ramírez-Mejía, D., Bowden, J., Ghilardi, A., & West, J. J. (2021). Limitations of WRF land surface models for simulating land use and land cover change in Sub-Saharan Africa and development of an improved model (CLM-AF v. 1.0). *Geoscientific Model Development*, *14*(6), 3215–3249. https://doi.org/10.5194/gmd-14-3215-2021

Gochis, D., Barlage, M., Cabell, R., Casali, M., Dugger, A., FitzGerald, K., et al. (2020). The WRF-Hydro® modeling system technical description (version 5.2) [Software]. *NCAR Technical Note*, 108. https://ral.ucar.edu/sites/default/files/public/projects/wrf-hydro/technical-description-user-guide/wrf-hydrov5.2technicaldescription.pdf

Grassi, G., House, J., Dentener, F., Federici, S., den Elzen, M., & Penman, J. (2017). The key role of forests in meeting climate targets requires science for credible mitigation. *Nature Climate Change*, *7*(3), 220–226. https://doi.org/10.1038/nclimate3227

Grell, G. A., & Freitas, S. R. (2014). A scale and aerosol aware stochastic convective parameterization for weather and air quality modeling. *Atmospheric Chemistry and Physics*, *14*(10), 5233–5250. https://doi.org/10.5194/acp-14-5233-2014

Griscom, B. W., Adams, J., Ellis, P. W., Houghton, R. A., Lomax, G., Miteva, D. A., et al. (2017). Natural climate solutions. *Proceedings of the National Academy of Sciences*, *114*(44), 11645–11650. https://doi.org/10.1073/pnas.1710465114

Guug, S., Sy, S., Quansah, E., Bliefernicht, J., Neidl, F., Steinbrecher, R., et al. (2025). Methane emissions from rice cultivation in West Africa and compensation options from nature reserve forests. *Environmental Research Letters*, *20*(4), 044050. https://doi.org/10.1088/1748-9326/adc28c

Harper, A. B., Powell, T., Cox, P. M., House, J., Huntingford, C., Lenton, T. M., et al. (2018). Land-use emissions play a critical role in land-based mitigation for Paris climate targets. *Nature Communications*, *9*(1), 2938. https://doi.org/10.1038/s41467-018-05340-z

Herrmann, S. M., Anyamba, A., & Tucker, C. J. (2005). Recent trends in vegetation dynamics in the African Sahel and their relationship to climate. *Global Environmental Change*, *15*(4), 394–404. https://doi.org/10.1016/j.gloenvcha.2005.08.004

Hersbach, H., Bell, B., Berrisford, P., Hirahara, S., Horányi, A., Muñoz-Sabater, J., et al. (2020). The ERA5 global reanalysis. *Quarterly Journal of the Royal Meteorological Society*, *146*(730), 1999–2049. https://doi.org/10.1002/qj.3803

Hingerl, L., Bliefernicht, J., Guug, S., Sy, S., Neidl, F., Jagdhuber, T., & Kunstmann, H. (2025). Comparative analysis of land–atmosphere interactions across three contrasting ecosystems in the West Sudanian savanna. *Journal of Hydrology: Regional Studies*, *61*, 102751. https://doi.org/10.1016/j.ejrh.2025.102751

Hirsch, A. L., Guillod, B. P., Seneviratne, S. I., Beyerle, U., Boysen, L. R., Brovkin, V., et al. (2018). Biogeophysical impacts of land-use change on climate extremes in low-emission scenarios: Results from HAPPI-land. *Earth's Future*, *6*(3), 396–409. https://doi.org/10.1002/2017EF000744

Hohenegger, C., Brockhaus, P., Bretherton, C. S., & Schär, C. (2009). The soil moisture–precipitation feedback in simulations with explicit and parameterized convection. *Journal of Climate*, *22*(19), 5003–5020. https://doi.org/10.1175/2009JCLI2604.1

Ingrosso, R., & Pausata, F. S. R. (2024). Contrasting consequences of the Great Green Wall: Easing aridity while increasing heat extremes. *One Earth*, *7*(3), 455–472. S2590332224000393. https://doi.org/10.1016/j.oneear.2024.01.017

IPCC-SRCCL. (2019). P. R. Shukla, J. Skeg, E. Calvo Buendia, V. Masson-Delmotte, H.-O. Pörtner, D. C. Roberts, et al. (Eds.), *Climate change and land: An IPCC special report on climate change, desertification, land degradation, sustainable land management, food security, and greenhouse gas fluxes in terrestrial ecosystems, Chapter 2* (p. 118). IPCC.

IPCC-SREX. (2012). *Managing the risks of extreme events and disasters to advance climate change adaptation: Special report of the intergovernmental panel on climate change* (1st ed.). Cambridge University Press. https://doi.org/10.1017/CBO9781139177245

Jia, G., Shevliakova, E., Artaxo, P., Noblet-Ducoudré, N. D., Houghton, R., Anderegg, W., et al. (2019). SPM2 Land–climate interactions.

Jungandreas, L., Hohenegger, C., & Claussen, M. (2023). How does the explicit treatment of convection alter the precipitation–soil hydrology interaction in the mid-holocene African humid period? *Climate of the Past*, *19*(3), 637–664. https://doi.org/10.5194/cp-19-637-2023

Jury, M. R. (2018). Climatic modulation of early summer dust emissions over West Africa. *Journal of Arid Environments*, *152*, 55–68. https://doi.org/10.1016/j.jaridenv.2018.01.019

Laux, P., Nguyen, P. N. B., Cullmann, J., Van, T. P., & Kunstmann, H. (2017). How many RCM ensemble members provide confidence in the impact of land-use land cover change? *International Journal of Climatology*, *37*(4), 2080–2100. https://doi.org/10.1002/joc.4836

Lehner, B., Verdin, K., & Jarvis, A. (2008). Hydrological data and maps based on SHuttle elevation derivatives at multiple scales-HydroSHEDS. Recuperado de Retrieved from https://www.Hydrosheds.Org

Lejeune, Q., Davin, E. L., Gudmundsson, L., Winckler, J., & Seneviratne, S. I. (2018). Historical deforestation locally increased the intensity of hot days in northern mid-latitudes. *Nature Climate Change*, *8*(5), 386–390. https://doi.org/10.1038/s41558-018-0131-z

Li, Y., De Noblet-Ducoudré, N., Davin, E. L., Motesharrei, S., Zeng, N., Li, S., & Kalnay, E. (2016). The role of spatial scale and background climate in the latitudinal temperature response to deforestation. *Earth System Dynamics*, *7*(1), 167–181. https://doi.org/10.5194/esd-7-167-2016

Lorenz, R., Pitman, A. J., & Sisson, S. A. (2016). Does Amazonian deforestation cause global effects; can we be sure? *Journal of Geophysical Research: Atmospheres*, *121*(10), 5567–5584. https://doi.org/10.1002/2015JD024357

Luo, X., Ge, J., Guo, W., Fan, L., Chen, C., Liu, Y., & Yang, L. (2022). The biophysical impacts of deforestation on precipitation: Results from the CMIP6 model intercomparison. *Journal of Climate*, *35*(11), 3293–3311. https://doi.org/10.1175/JCLI-D-21-0689.1

Luyssaert, S., Jammet, M., Stoy, P. C., Estel, S., Pongratz, J., Ceschia, E., et al. (2014). Land management and land-cover change have impacts of similar magnitude on surface temperature. *Nature Climate Change*, *4*(5), 389–393. https://doi.org/10.1038/nclimate2196

Mahmood, R., Pielke, R. A., Sr., Hubbard, K. G., Niyogi, D., Dirmeyer, P. A., McAlpine, C., et al. (2014). Land cover changes and their biogeophysical effects on climate. *International Journal of Climatology*, *34*(4), 929–953. https://doi.org/10.1002/joc.3736

Masih, I., Maskey, S., Mussá, F. E. F., & Trambauer, P. (2014). A review of droughts on the African continent: A geospatial and long-term perspective. *Hydrology and Earth System Sciences*, *18*(9), 3635–3649. https://doi.org/10.5194/hess-18-3635-2014

Mortey, E. M., Arnault, J., Inoussa, M. M., Madougou, S., Annor, T., Laux, P., et al. (2024). Regional climate response to land cover change in Tropical West Africa: A numerical sensitivity experiment with esa land cover data and advanced wrf-hydro. *Frontiers in Water*, *6*, 1372333. https://doi.org/10.3389/frwa.2024.1372333

Muñoz-Sabater, J., Dutra, E., Agustí-Panareda, A., Albergel, C., Arduini, G., Balsamo, G., et al. (2021). ERA5-Land: A state-of-the-art global reanalysis dataset for land applications. *Earth System Science Data*, *13*(9), 4349–4383. https://doi.org/10.5194/essd-13-4349-2021

Nadolski, L., Bliefernicht, J., Petrovic, D., Rauch, M., SY, S., Guug, S., et al. (2024). Exploring and closing the energy balance of eddy covariance measurements along a land use gradient in the West African Sudanian savanna. *Frontiers in Water*, *6*, 1393884. https://doi.org/10.3389/frwa.2024.1393884

Ndiaye, A., Camara, M., Sy, S., Mamadou Lamine, M., Arnault, J., Kunstmann, & Haral, H. (2024). Potential contribution of land cover change on flood events in the Senegal River basin. *Frontiers in Water*, *6*, 1447577. https://doi.org/10.3389/frwa.2024.1447577

Nicholson, S. E. (2013). The West African Sahel: A review of recent studies on the rainfall regime and its interannual variability. *International Scholarly Research Notices*, *2013*, e453521–e453532. https://doi.org/10.1155/2013/453521

Niu, G.-Y., Yang, Z.-L., Mitchell, K. E., Chen, F., Ek, M. B., Barlage, M., et al. (2011). The community Noah land surface model with multiparameterization options (Noah-MP): 1. Model description and evaluation with local-scale measurements. *Journal of Geophysical Research*, *116*(D12), D12109. https://doi.org/10.1029/2010JD015139

de Noblet-Ducoudré, N., Boisier, J.-P., Pitman, A., Bonan, G. B., Brovkin, V., Cruz, F., et al. (2012). Determining robust impacts of land-use-induced land cover changes on surface climate over North America and Eurasia: Results from the first set of LUCID experiments. https://doi.org/10.1175/JCLI-D-11-00338.1

Nyadzi, E., Werners, S. E., Biesbroek, R., & Ludwig, F. (2022). Towards weather and climate services that integrate indigenous and scientific forecasts to improve forecast reliability and acceptability in Ghana. *Environmental Development*, *42*, 100698. https://doi.org/10.1016/j.envdev.2021.100698

Odoulami, R. C., Abiodun, B. J., & Ajayi, A. E. (2019). Modelling the potential impacts of afforestation on extreme precipitation over West Africa. *Climate Dynamics*, *52*(3), 2185–2198. https://doi.org/10.1007/s00382-018-4248-6

Pall, P., Allen, M. R., & Stone, D. A. (2007). Testing the Clausius–Clapeyron constraint on changes in extreme precipitation under CO2 warming. *Climate Dynamics*, *28*(4), 351–363. https://doi.org/10.1007/s00382-006-0180-2

Palmer, L. (2021). How trees and forests reduce risks from climate change. *Nature Climate Change*, *11*(5), 374–377. https://doi.org/10.1038/s41558-021-01041-6

Park, H., Hwang, J., Cha, D.-H., Lee, M.-I., Song, C.-K., Kim, J., et al. (2024). Does a scale-aware convective parameterization scheme improve the simulation of heavy rainfall events? *Journal of Geophysical Research: Atmospheres*, *129*(7), e2023JD039407. https://doi.org/10.1029/2023JD039407

Park, H., Kim, G., Cha, D.-H., Chang, E.-C., Kim, J., Park, S.-H., & Lee, D.-K. (2022). Effect of a scale-aware convective parameterization scheme on the simulation of convective cells-related heavy rainfall in South Korea. *Journal of Advances in Modeling Earth Systems*, *14*(6), e2021MS002696. https://doi.org/10.1029/2021MS002696

Pausata, F. S. R., Gaetani, M., Messori, G., Berg, A., Souza, D. M., Sage, R. F., & de Menocal, P. B. (2020). The greening of the Sahara: Past changes and future implications. *One Earth*, *2*(3), 235–250. https://doi.org/10.1016/j.oneear.2020.03.002

Perugini, L., Caporaso, L., Marconi, S., Cescatti, A., Quesada, B., de Noblet-Ducoudré, N., et al. (2017). Biophysical effects on temperature and precipitation due to land cover change. *Environmental Research Letters*, *12*(5), 053002. https://doi.org/10.1088/1748-9326/aa6b3f

Pongratz, J., Reick, C. H., Raddatz, T., & Claussen, M. (2010). Biogeophysical versus biogeochemical climate response to historical anthropogenic land cover change. *Geophysical Research Letters*, *37*(8). https://doi.org/10.1029/2010GL043010

Potapov, P., Turubanova, S., Hansen, M. C., Tyukavina, A., Zalles, V., Khan, A., et al. (2022). Global maps of cropland extent and change show accelerated cropland expansion in the twenty-first century. *Nature Food*, *3*(1), 19–28. https://doi.org/10.1038/s43016-021-00429-z

Quesada, B., Devaraju, N., de Noblet-Ducoudré, N., & Arneth, A. (2017). Reduction of monsoon rainfall in response to past and future land use and land cover changes. *Geophysical Research Letters*, *44*(2), 1041–1050. https://doi.org/10.1002/2016GL070663

Rahimi, J., Ago, E. E., Ayantunde, A., Berger, S., Bogaert, J., Butterbach-Bahl, K., et al. (2021). Modeling gas exchange and biomass production in West African Sahelian and Sudanian ecological zones. *Geoscientific Model Development*, *14*(6), 3789–3812. https://doi.org/10.5194/gmd-14-3789-2021

Rosenstock, T. S., Lamanna, C., Chesterman, S., Bell, P., Arslan, A., Richards, M. B., et al. (2016). The scientific basis of climate-smart agriculture: A systematic review protocol. Retrieved from https://hdl.handle.net/10568/70967

Rummler, T., Arnault, J., Gochis, D., & Kunstmann, H. (2019). Role of lateral terrestrial water flow on the regional water cycle in a complex terrain region: Investigation with a fully coupled model system. *Journal of Geophysical Research: Atmospheres*, *124*(2), 507–529. https://doi.org/10.1029/2018JD029004

Salack, S., Saley, I. A., Lawson, N. Z., Zabré, I., & Daku, E. K. (2018). Scales for rating heavy rainfall events in the West African Sahel. *Weather and Climate Extremes*, *21*, 36–42. https://doi.org/10.1016/j.wace.2018.05.004

Saley, I. A., Salack, S., Sanda, I. S., Moussa, M. S., Bonkaney, A. L., Ly, M., & Fodé, M. (2019). The possible role of the Sahel Greenbelt on the occurrence of climate extremes over the West African Sahel. *Atmospheric Science Letters*, *20*(8), e927. https://doi.org/10.1002/asl.927

Sanogo, S., Fink, A., Omotosho, J., Abdramane, B., Redl, R., & Ermert, V. (2015). Spatio-temporal characteristics of the recent rainfall recovery in West Africa. *International Journal of Climatology*, *35*(15), 4589–4605. https://doi.org/10.1002/joc.4309

Savitzky, A., & Golay, M. J. E. (1964). Smoothing and differentiation of data by simplified least squares procedures. *Analytical Chemistry*, *36*(8), 1627–1639. https://doi.org/10.1021/ac60214a047

Schwaab, J., Davin, E. L., Bebi, P., Duguay-Tetzlaff, A., Waser, L. T., Haeni, M., & Meier, R. (2020). Increasing the broad-leaved tree fraction in European forests mitigates hot temperature extremes. *Scientific Reports*, *10*(1), 14153. https://doi.org/10.1038/s41598-020-71055-1

Seneviratne, S. I., Corti, T., Davin, E. L., Hirschi, M., Jaeger, E. B., Lehner, I., et al. (2010). Investigating soil moisture–climate interactions in a changing climate: A review. *Earth-Science Reviews*, *99*(3), 125–161. https://doi.org/10.1016/j.earscirev.2010.02.004

Sillmann, J., Kharin, V. V., Zhang, X., Zwiers, F. W., & Bronaugh, D. (2013). Climate extremes indices in the CMIP5 multimodel ensemble: Part 1. Model evaluation in the present climate. *Journal of Geophysical Research: Atmospheres*, *118*(4), 1716–1733. https://doi.org/10.1002/jgrd.50203

Skamarock, W. C., Klemp, J. B., Dudhia, J., Gill, D. O., Liu, Z., Berner, J., et al. (2019). A description of the advanced research WRF version 4. *NCAR Tech. Note Ncar/Tn-556+ Str*, 145.

Smets, B., Jacobs, T., & Verger, A. (2018). Product user manual: Leaf area index (LAI), fraction of photosynthetically active radiation (FAPAR), fraction of vegetation cover (FCover), collection 300 m (version 1, issue I1.60). Retrieved from https://land.copernicus.eu/en/technical-library/product-user-manual-leaf-area-index-333-m-version-1/

Smiatek, G., & Kunstmann, H. (2023). Potential impact of the Pan-African great green wall on Sahelian Summer precipitation: A global Modeling approach with MPAS. *Earth Interactions*, *27*(1). https://doi.org/10.1175/EI-D-22-0013.1

Spracklen, D. V., Baker, J. C. A., Garcia-Carreras, L., & Marsham, J. H. (2018). The effects of tropical vegetation on rainfall. *Annual Review of Environment and Resources*, *43*(1), 193–218. https://doi.org/10.1146/annurev-environ-102017-030136

Sulla-Menashe, D., Gray, J. M., Abercrombie, S. P., & Friedl, M. A. (2019). Hierarchical mapping of annual global land cover 2001 to present: The MODIS collection 6 land cover product. *Remote Sensing of Environment*, *222*, 183–194. https://doi.org/10.1016/j.rse.2018.12.013

Sy, S. (2025). Model output data for WRF-hydro simulations used in this study [Dataset]. *Zenodo*. https://doi.org/10.5281/zenodo.14876696

Sy, S., Madonna, F., Rosoldi, M., Tramutola, E., Gagliardi, S., Proto, M., & Pappalardo, G. (2021). Sensitivity of trends to estimation methods and quantification of subsampling effects in global radiosounding temperature and humidity time series. *International Journal of Climatology*, *41*(S1), E1992–E2014. https://doi.org/10.1002/joc.6827

Sy, S., Noblet-Ducoudré, N. D., Quesada, B., Sy, I., Dieye, A. M., Gaye, A. T., & Sultan, B. (2017). Land-surface characteristics and climate in West Africa: Models' biases and impacts of historical anthropogenically-induced deforestation. *Sustainability*, *9*(10), 1917. https://doi.org/10.3390/su9101917

Sy, S., & Quesada, B. (2020). Anthropogenic land cover change impact on climate extremes during the 21st century. *Environmental Research Letters*, *15*(3), 034002. https://doi.org/10.1088/1748-9326/ab702c

Sylla, M. B., Nikiema, P. M., Gibba, P., Kebe, I., & Klutse, N. A. B. (2016). Climate change over West Africa: Recent trends and future projections. *Adaptation to Climate Change and Variability in Rural West Africa*, 25–40. https://doi.org/10.1007/978-3-319-31499-0_3

Taylor, C. M., Birch, C. E., Parker, D. J., Dixon, N., Guichard, F., Nikulin, G., & Lister, G. M. S. (2013). Modeling soil moisture-precipitation feedback in the Sahel: Importance of spatial scale versus convective parameterization. *Geophysical Research Letters*, *40*(23), 6213–6218. https://doi.org/10.1002/2013GL058511

Teuling, A. J., Taylor, C. M., Meirink, J. F., Melsen, L. A., Miralles, D. G., van Heerwaarden, C. C., et al. (2017). Observational evidence for cloud cover enhancement over western European forests. *Nature Communications*, *8*(1), 14065. https://doi.org/10.1038/ncomms14065

UNCCD. (2024). Great green wall initiative. *United Nations Convention to Combat Desertifcation*. Retrieved from https://www.unccd.int/our-work/ggwi

Wang, G., Yu, M., & Xue, Y. (2016). Modeling the potential contribution of land cover changes to the late twentieth century Sahel drought using a regional climate model: Impact of lateral boundary conditions. *Climate Dynamics*, *47*(11), 3457–3477. https://doi.org/10.1007/s00382-015-2812-x

Waongo, M., Laux, P., Coulibaly, A., Sy, S., & Kunstmann, H. (2024). Assessing the impacts of climate change on rainfed maize production in Burkina Faso, West Africa. *Atmosphere*, *15*(12), 1438. https://doi.org/10.3390/atmos15121438

Winckler, J., Reick, C. H., & Pongratz, J. (2017). Robust identification of local biogeophysical effects of land-cover change in a global climate model. *Journal of Climate*, *30*(3), 1159–1176. https://doi.org/10.1175/JCLI-D-16-0067.1

Windisch, M. G., Davin, E. L., & Seneviratne, S. I. (2021). Prioritizing forestation based on biogeochemical and local biogeophysical impacts. *Nature Climate Change*, *11*(10), 867–871. https://doi.org/10.1038/s41558-021-01161-z

Wolfs, D., Verger, A., Van der Goten, R., & Sánchez-Zapero, J. (2022). Product user manual: Leaf area index (LAI), fraction of absorbed photosynthetically active radiation (FAPAR), fraction of green vegetation cover (FCover), collection 300 m (version 1.1, issue I1.20). Retrieved from https://land.copernicus.eu/en/technical-library/product-user-manual-leaf-area-index-333-m-version-1-1/

Wu, P., Han, Y., Chen, T., & Tu, X. m. (2014). Causal inference for mann–whitney–wilcoxon rank sum and other nonparametric statistics. *Statistics in Medicine*, *33*(8), 1261–1271. https://doi.org/10.1002/sim.6026

Yahaya Seydou, A. N., Sy, S., Quesada, B., Bliefernicht, J., Manevski, K., Amekudzi, L. K., et al. (2025). Biophysical effects of land cover changes in West Africa: A systematic review. *Environmental Research Letters*, *20*(7), 073001. https://doi.org/10.1088/1748-9326/addbf4

Zeng, Z., Wang, D., Yang, L., Wu, J., Ziegler, A. D., Liu, M., et al. (2021). Deforestation-induced warming over tropical mountain regions regulated by elevation. *Nature Geoscience*, *14*(1), 23–29. https://doi.org/10.1038/s41561-020-00666-0